Marine and Petroleum Geology 182 (2025) 107559

Contents lists available at ScienceDirect

Marine and Petroleum Geology

journal homepage: www.elsevier.com/locate/marpetgeo

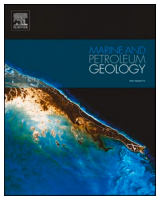

Multidisciplinary characterization of migrated bitumen enrichment and pore network development in low-maturity Es_4 shales of the Damintun Sag, East China

Yong Ma [a], Qinhong Hu [b], Jianbin Xu [c], Binhao Feng [a], Fujie Jiang [a], Yanshan Wang [c], Haiping Huang [d,e,*]

[a] State Key Laboratory of Petroleum Resources and Engineering, China University of Petroleum (Beijing), Changping, Beijing, 102249, China
[b] National Key Laboratory of Deep Oil and Gas, China University of Petroleum (East China), Qingdao, 266580, China
[c] Exploration and Development Research Institute, PetroChina Liaohe Oilfield Company, Liaohe, Panjin, 124010, China
[d] School of Geosciences, Yangtze University, Wuhan, 430100, Hubei, China
[e] Department of Earth, Energy, and Environment, University of Calgary, Calgary, T2N 1N4, Canada

A B S T R A C T

Low-maturity shale oil resources are widely developed in the Paleogene-aged Damintun Sag of the Bohai Bay Basin, yet the unclear pore architecture and reservoir space distribution have hindered its efficient exploitation. Focusing on the low-maturity Es_4 shale, this study integrates core observations, geochemical tests, X-ray diffraction, scanning electron microscopy (SEM), and mercury intrusion porosimetry (MIP) data from Well S352 to investigate lithofacies-controlled pore structures and residual oil characteristics. Three lithofacies reservoirs are identified: laminated felsic shale (LFS), mixed shale (MS), and massive dolomitic mudstone (MDM). LFS and MS are rich in Type I kerogen excellent hydrocarbon generation and retention. LFS acts as both source and reservoir rock, featuring abundant mesopores, strong pore connectivity, and bedding-parallel fractures, making it a favorable sweet spot for *in situ* generation and light oil expulsion. MS serves as a transitional facies with moderate generative and physical properties. In contrast, MDM, with low TOC and poor pore connectivity, lacks generative capacity and instead functions as a secondary reservoir that stores migrated oil from adjacent LFS. Thermal maturity assessments show high T_{max} values (up to 465 °C) indicative of peak oil generation, despite low measured R_o (~0.6 %), likely suppressed by algal kerogen. Multiscale pore analyses reveal that LFS contains the highest cumulative pore volume and most developed pore–fracture networks, while MDM exhibits isolated, diagenetically altered pores. Geochemical zonation and gas chromatography fingerprinting distinguishes indigenous hydrocarbons in LFS/MS from migrated oils in MDM, confirming stratigraphically confined migration. Laminated shale—particularly those with interbedded MDM intervals—show optimal conditions for sweet spot development, as short-range migration enriches reservoir potential without requiring high maturity. This study underscores the viability of low-maturity shale oil systems and emphasizes the importance of integrating lithofacies, geochemistry, and pore network architecture to predict sweet spots for optimized exploration in lacustrine shale formations.

1. Introduction

Shale oil has revolutionized the global energy landscape, primarily due to advances in horizontal drilling, hydraulic fracturing, and reservoir characterization (Malozyomov et al., 2023). The U.S. leads this shift with major production from marine-origin formations like the Wolfcamp and Spraberry in the Permian Basin, the Bakken, and the Eagle Ford, which together contribute over 70 % of global shale oil output (Nalley and LaRose, 2021). Other nations, such as Argentina (Vaca Muerta) and Russia (Bazhenov), have also achieved notable progress (Salygin et al., 2019). A critical control on shale oil productivity is thermal maturity, typically measured by vitrinite reflectance (Ro), which affects hydrocarbon generation, oil viscosity, and mobility (Cardott, 2012; Jarvie, 2012; Zhao et al., 2020). In formations like Alberta's Duvernay (R_o 0.99–1.32 %) and the Midland Basin's Wolfcamp and Spraberry (R_o > 0.9 %), productivity aligns closely with maturity levels, showing local expulsion dominance over long-range migration (Van de Wetering et al., 2016; Drake et al., 2019). Similarly, Eagle Ford production improves markedly above R_o 0.85 % due to better fracture development (Hou et al., 2021).

In recent years, China has emerged as a significant player in shale oil exploration and development. High-maturity plays have been successfully established in the Ordos Basin, Junggar Basin, the Qingshankou Formation in the Songliao Basin, and the Kongdian Formation in the Bohai Bay Basin, where R_o typically ranges from 0.9 % to 1.3 % (Wang et al., 2022; Yang et al., 2023). However, a substantial

* Corresponding author. School of Geosciences, Yangtze University, Wuhan, 430100, Hubei, China.
E-mail address: huah@ucalgary.ca (H. Huang).

https://doi.org/10.1016/j.marpetgeo.2025.107559
Received 22 May 2025; Received in revised form 10 July 2025; Accepted 12 July 2025
Available online 14 July 2025

portion—estimated at 60–70 %—of China's technically recoverable shale oil resources is hosted in moderately to low-maturity lacustrine shales (R_o < 1.0 %), such as the Shahejie Formation in the Bohai Bay Basin and the Nenjiang Formation in the Songliao Basin (Zhao et al., 2020; Ma et al., 2022). These lacustrine systems differ from marine shales in several important ways, including depositional environments, organic matter types (often Type I), and stronger vertical and lateral lithological heterogeneity (Jin et al., 2021). Despite relatively low thermal maturity, recent breakthroughs in China have demonstrated the economic potential of shale oil production under favorable geological conditions. In the Jiyang Depression of the Bohai Bay Basin, shales in the Es_4 and Es_3 submembers (R_o 0.7 %–1.0 %) have shown promising results, with Well Niuxie-124 (R_o 0.6 %–0.7 %) producing over 40 tonnes/day (t/d) and Well FEY1-1HF achieving a national record of 262.8 t/d (Wang et al., 2024; Yang et al., 2024). Similarly, Well Shen 224 in the Es_4 Member of the Liaohe Depression tested at 6.2 t/d, highlighting the potential of low-to medium-maturity shales (Chen et al., 2015). In the Songliao Basin, the Nenjiang Formation (R_o 0.5 %–0.8 %) holds over 1 billion tons of estimated shale oil resources, with Well NY1H confirming its productivity by yielding 2160 tons over 424 days at a steady rate of 8.6 t/d (He et al., 2024).

Despite these encouraging results, the mechanisms behind shale oil enrichment in moderately low-maturity lacustrine settings remain inadequately understood. Key factors such as organic matter abundance, fracture systems, mineralogical composition, overpressure development, and particularly lithofacies architecture are known to affect oil accumulation (Jiang et al., 2020; Hu et al., 2022). Recent studies point to the critical role of micro-scale oil migration within the shale itself—typically from organic-rich laminae into adjacent organic-lean or carbonate-rich layers, forming micro-reservoirs within highly heterogeneous strata (Hu et al., 2025). In these systems, even limited expulsion at low maturity can lead to localized oil accumulations if migration pathways and storage space are available. Fractures and overpressure conditions further assist hydrocarbon redistribution within tight systems, overcoming poor mobility constraints commonly associated with low R_o values (Liu et al., 2023).

The Damintun Sag in the Liaohe Depression of the Bohai Bay Basin offers a representative setting to investigate low-maturity shale oil systems. The fourth member of the Shahejie Formation (Es_4 Member) comprises organic-rich lacustrine shales with vitrinite reflectance (R_o) values generally below 1.0 %, which have been shown to yield commercial volumes of oil (Chen et al., 2015, 2017; Li X. et al., 2019). These shales are characterized by high total organic carbon (TOC) content and the presence of high molecular weight hydrocarbons, contributing to the generation of high-wax oils. Despite this resource potential, there remain significant challenges in understanding the mechanisms of hydrocarbon retention and migration, particularly given the relatively low thermal maturity. Accurate characterization of pore structures, reservoir quality, and micro-migration behavior is limited by the complex lithofacies heterogeneity and nano-scale pore systems.

This study seeks to bridge existing knowledge gaps through an integrated geological and geochemical approach. By combining whole-rock mineralogy, organic geochemistry, field emission-scanning electron microscopy (FE-SEM), X-ray computed tomography (CT), mercury intrusion porosimetry (MIP), and regional geological data, we systematically evaluate shale distribution, source rock quality, oil content, and reservoir architecture in the Es_4 Member. Emphasis is placed on lithofacies classification, source–reservoir coupling, and lithofacies-controlled micro-migration to clarify the interactions among mineral composition, organic matter distribution, and pore network development. The ultimate objective is to establish a conceptual model of low-maturity shale oil enrichment and improve sweet spot prediction in the Damintun Sag and similar lacustrine rift basins.

2. Geological setting and analytical methods

2.1. Geological setting

The Damintun Sag, located in the northernmost part of the Liaohe Depression within the Bohai Bay Basin, is a Mesozoic–Cenozoic extensional structure shaped by Paleogene rifting. It forms a NE-trending, fault-controlled triangle-shaped depression—broad in the south and narrow in the north—covering approximately 800 km^2 (Fig. 1). Its evolution is associated with dextral strike-slip motion along the Tan-Lu fault, resulting in a complex pattern of grabens and half-grabens (Guo et al., 2016). Secondary structural features within the sag are controlled by main boundary faults and include three uplifts and three sub-sags: Santaizi, Anfutun, and Rongshengbao sub-sags, and the Central, Western, and Biantai-Fahaniu uplifts (Chen et al., 2015; Guo et al., 2016). The sag is underlain and surrounded by Archean granite-gneiss and Proterozoic carbonate rocks, overlain unconformably by the thick Eocene Shahejie (Es) Formation, which is stratigraphically divided into four members (Es_4–Es_1), though Es_2 is absent locally (Huang et al., 2003; Hao et al., 2009; Chen et al., 2020). These Archean granite-gneiss and Proterozoic carbonate rocks also contributed to the provenance of the Mesozoic–Cenozoic strata in the Damintun Sag (Guo et al., 2016; Chen et al., 2020).

The Damintun Sag features thick Paleogene lacustrine successions primarily from the Shahejie and Dongying (Ed) formations, with the Es_4 and Es_3 members serving as the main source rocks. These units consist of organic-rich dark mudstones and shales deposited under anoxic lake conditions and contain predominantly Type I and II kerogen, with TOC ranging from 1.5 % to 6 %, reflecting strong oil and gas generation potential (Li X. et al., 2019). Reservoirs are mainly found in the Es_3 and Es_1 members, comprising fine-to medium-grained sandstones interbedded with shales, forming classic source-reservoir-seal systems with structural, stratigraphic, and lithologic traps. Effective cap rocks consist of thick mudstones and evaporites in the upper Es and Ed formations, providing excellent vertical sealing (Hao et al., 2009). Among the Shahejie units, the Es_4 Member plays a pivotal role in hydrocarbon generation (,Li X. et al., 2019; Chen et al., 2020), having been deposited during a phase of progressive lacustrine transgression driven by active rifting and subsidence in the Bohai Bay Basin. Initial deposition occurred in shore-shallow lacustrine facies within semi-graben settings, influenced by faulting and basement tilting (Chen et al., 2015). As subsidence intensified, the environment transitioned to semi-deep and deep lacustrine settings, coinciding with peak transgression and maximum organic matter accumulation. A warm, humid, and reducing climate fostered high biological productivity, particularly algae, bacteria, and plankton in brackish waters, resulting in extensive deposition of dark, organic-rich shales in the lower Es_4, which now represents the principal target for shale oil (Chen et al., 2015; Li X. et al., 2019).

Core studies from Well S352 in the Anfutun sub-sag further highlight the shale oil potential within Es_4. The vertical profile is subdivided into three lithological intervals (Li H. et al., 2019). Interval I consists of gray to dark gray oil shales with minor mudstone interbeds, deposited under relatively anoxic conditions. Interval II features a thick layer of grayish-green argillaceous dolomite, pointing to chemically variable environments, possibly with episodic evaporation. Interval III is composed of black oil shales interbedded with thin dolomitic layers, indicating deep, stratified lacustrine settings rich in preserved organic matter. The Damintun Sag thus presents a favorable geological setting for both conventional accumulations and growing unconventional shale oil potential, particularly within the Es_4 Member's low-to medium--maturity zones (Chen et al., 2020).

2.2. Methods

2.2.1. X-ray diffraction (XRD)

The mineralogical composition of shale samples was determined

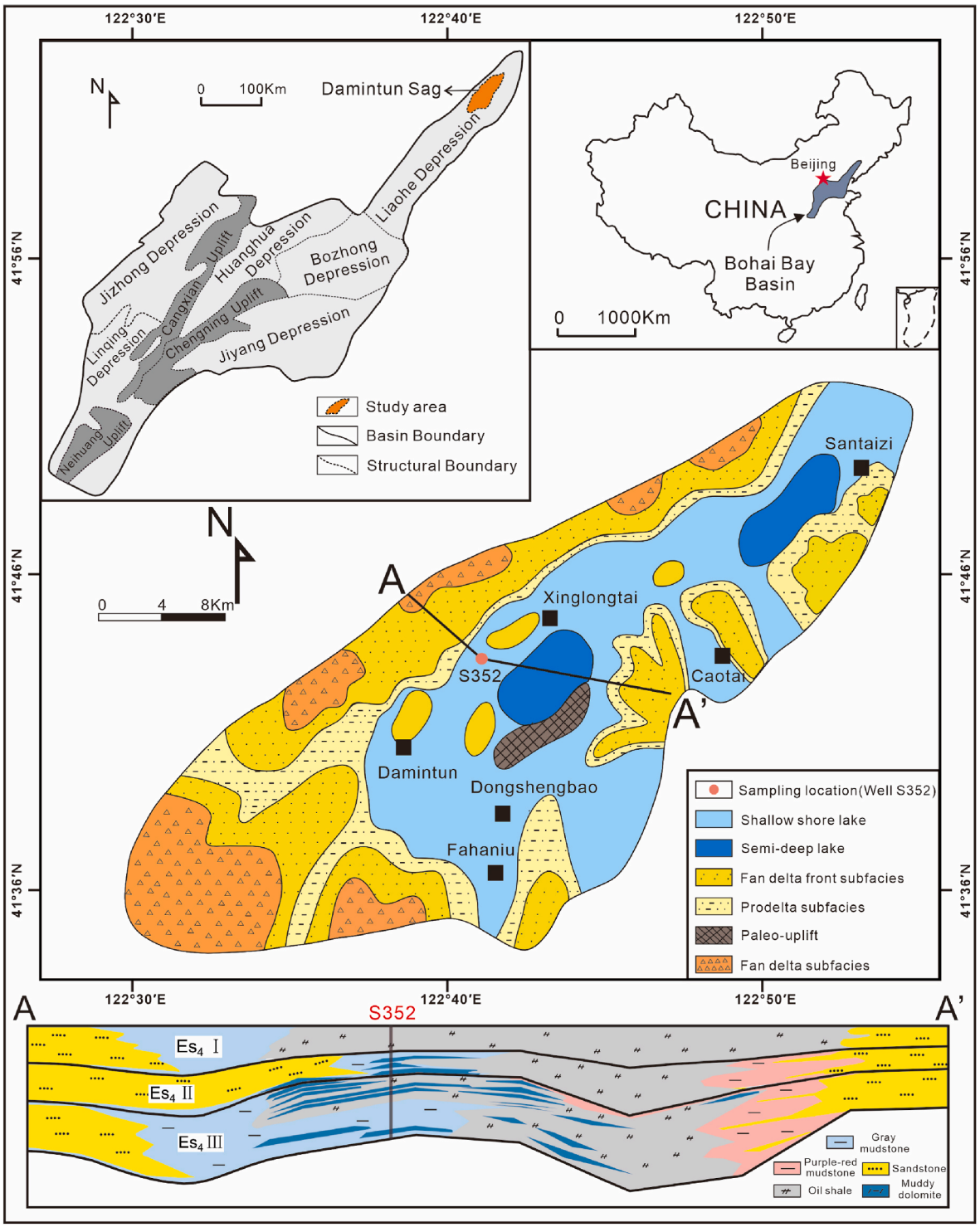

Fig. 1. Structural framework of the Bohai Bay Basin illustrating the sedimentary facies distribution of the E_{s4} Member of the Paleogene Shahejie Formation and the location of Well S352 within the Damintun Sag (modified from Li X. et al., 2019).

using a Bruker D8 Discover powder X-ray diffractometer with a Cu Kα radiation source (λ = 1.5418 Å). Approximately 10 g of homogenized sample powder was mixed with ethanol and finely ground using an agate mortar to a particle size below 10 μm. The suspension was smear-mounted onto glass slides to minimize preferred orientation effects. Diffraction patterns were collected at 40 kV and 30 mA across a 2θ range of 3–70°, with a 0.02° step size and 1 s/step acquisition time. Phase identification and semi-quantitative analysis were conducted using Bruker AXS Topas® V7.0 software with Rietveld refinement.

2.2.2. *Scanning electron microscopy (SEM) and QEMSCAN analysis*

Shale specimens were mechanically polished using a Leica EM TXP system and further refined with ion beam milling (Leica EM RES102) at 3 kV for 6–10 h to obtain a smooth analytical surface. Samples were mounted on SEM stubs with carbon adhesive and coated with a conductive carbon layer. Microstructural imaging was performed using a ZEISS Merlin field-emission SEM (FE-SEM) at 1–2 kV with a 3.5–5.5 mm working distance to generate high-resolution backscattered electron (BSE) images. Quantitative mineralogical characterization was carried

out using the QEMSCAN system, which integrates dual Bruker Quantax EDS detectors with FE-SEM and AMICS software. Elemental and textural data were captured at 1 μm pixel resolution, enabling detailed mapping of mineral phases, particle size distributions, and textural relationships.

2.2.3. Focused ion beam-scanning electron microscopy (FIB-SEM)

Three-dimensional microstructural analysis was conducted using a ZEISS Crossbeam 540 FIB-SEM system. Pretreatment was consistent with QEMSCAN preparation protocols. Imaging parameters included a 2 kV electron beam, 2.5 nm beam spot size, and a 54° ion/electron beam angle. Sequential ion beam milling (20 nm slice thickness) and electron imaging were repeated for 500 cycles to construct a nanoscale 3D dataset (2048 × 1536 pixels). The resulting volume was processed in Avizo 9.0.1 for grayscale-based segmentation and 3D quantitative analysis of pore networks and organic matter distribution.

2.2.4. Rock-Eval pyrolysis

Rock-Eval pyrolysis was performed using an OGE-II instrument on powdered shale samples (<0.15 mm). Free hydrocarbons (S_1) were measured at 300 °C, while potential hydrocarbons (S_2) were released during heating from 300 °C to 650 °C. T_{max} values were used to assess thermal maturity. Hydrogen Index (HI), Oxygen Index (OI), and Production Index (PI) were calculated to evaluate organic matter quality. Calibration was conducted with certified reference materials to ensure analytical accuracy.

2.2.5. Optical microscopy

Hydrocarbon occurrence and morphology were examined using a ZEISS Axioscope 5 polarized light microscope. Samples were analyzed under orthogonal polarized light, violet fluorescence (excitation at 420 nm), and blue fluorescence (excitation at 470 nm) at 100 × and 200× magnifications. Observations focused on hydrocarbon morphology, distribution, and fluorescence characteristics.

2.2.6. X-ray micro-computed tomography (CT)

X-ray Micro-CT scanning was conducted using a Sanying nanoVoxel-3000 system at 80 kV, 40 μA, and 2 μm resolution. The 3D CT datasets were reconstructed and visualized in Avizo 9.0.1. Pore networks were extracted via grayscale histogram segmentation, enabling quantitative characterization of pore geometry and size distribution.

2.2.7. High-pressure mercury intrusion porosimetry (MIP)

Samples were dried at 110 °C for 24 h and degassed under vacuum (1×10^{-3} psi) prior to analysis. Mercury intrusion tests were carried out using a Micromeritics™ Autopore IV 9500 porosimeter across a pressure range of 1–60,000 psi, corresponding to pore diameters between 3 nm and 180 μm. Bulk and skeletal densities were measured at 1 psi and 60,000 psi, respectively. These data were used to calculate porosity and characterize pore size distribution across multiple scales.

3. Results

3.1. Lithofacies classification

Shale lithofacies—including bedding features and mineral composition, referred to as micro-facies in this study—were identified based on thin-section observations, QEMSCAN, and XRD analyses. To characterize the mineral composition of the Es_4 Member, a comprehensive XRD analysis was performed on 124 rock samples from Well S352. The dominant minerals identified include quartz (ranging from 2.7 % to 57.4 %, with an average of 34.5 %), clay minerals (0 %–48.2 %, avg. 31.6 %), dolomite (0 %–84.1 %, avg. 18.1 %), feldspar (0 %–44.4 %, avg. 6.3 %), and calcite (0 %–38.4 %, avg. 3.8 %) (Fig. 2). Trace amounts of pyrite (average ~ 3.8 %) were also detected, indicating localized reducing conditions during deposition. These mineralogical data reveal pronounced vertical variability across the stratigraphic section,

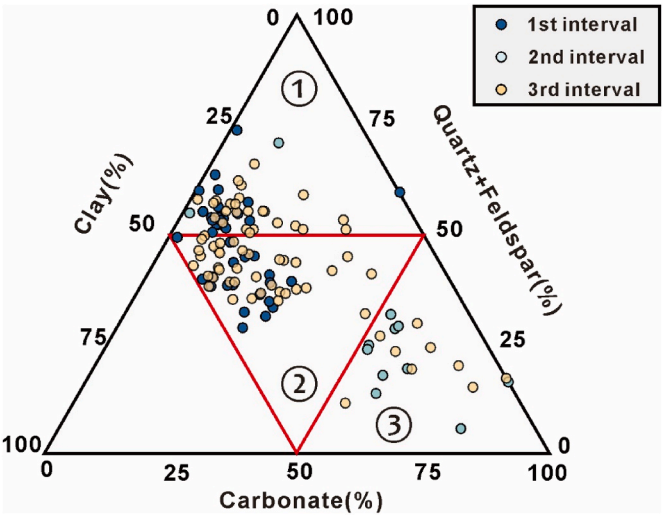

Fig. 2. Ternary diagram showing the mineral composition of shales from the Es_4 Member in the Damintun Sag, with lithofacies classified as (1) laminated felsic shale, (2) mixed shale, and (3) massive dolomitic mudstone.

underscoring the complexity of the depositional and diagenetic processes involved.

Lithology in the Es_4 Member was classified using a ternary diagram based on the relative proportions of felsic minerals, carbonate minerals, and clay minerals. This approach grouped the rocks into 12 basic shale lithologies: limestone, argillaceous limestone, felsic limestone, shale, calcareous shale, felsic shale, siltstone, argillaceous siltstone, calcareous siltstone, calcareous mixed shale, argillaceous mixed shale, and felsic mixed shale. Fig. 3 presents QEMSCAN mineralogical maps of three representative lithofacies that illustrate this classification. (A) Laminated felsic shale (LFS) at 3225 m is dominated by quartz (57.35 wt%), with notable albite (10.37 wt%) and dolomite (9.74 wt%), and minor amounts of chlorite, pyrite, and organic matter (0.35 wt%). Its fine-grained, laminated texture and silica-rich composition suggest deposition in a low-energy, oxidizing environment with moderate carbonate input. (B) Massive dolomitic mudstone (MDM) at 3248 m contains high dolomite (50.21 wt%) and quartz (36.96 wt%), but negligible pyrite and organic matter, with a compact, structureless matrix indicative of deposition under chemically influenced, likely evaporative conditions. (C) Laminated mixed shale (MS) at 3280 m exhibits a balanced mineral composition, including quartz (47.86 wt%), illite (26.91 wt%), dolomite (7.08 wt%), and minor calcite (3.33 wt%), along with higher organic content (0.84 wt%). Its finely laminated structure and intermediate mineralogy suggest deposition in a fluctuating redox environment with mixed sediment input. These mineralogical maps validate the lithofacies distinctions: lithofacies LFS is silica-dominated with moderate carbonates and low clay content; lithofacies MS has a mixed mineralogy with abundant clay and elevated organic matter; and lithofacies MDM is a carbonate-rich facies with poor organic preservation. Collectively, these facies reflect contrasting depositional conditions and play different roles in the source–reservoir system of the Es_4 Member.

The Es_4 Member can be subdivided into three distinct intervals based on key lithofacies characteristics. Interval I is dominated by LFS and MS, indicative of quiet, low-energy depositional environments. Interval II is primarily composed of MDM, reflecting more chemically influenced, evaporative conditions. Interval III features interbedded LFS, MS, and MDM, suggesting a more dynamic and variable depositional regime. These stratigraphic divisions are supported by lithological column data, with variations in organic matter content providing further criteria for facies differentiation, as discussed in later sections.

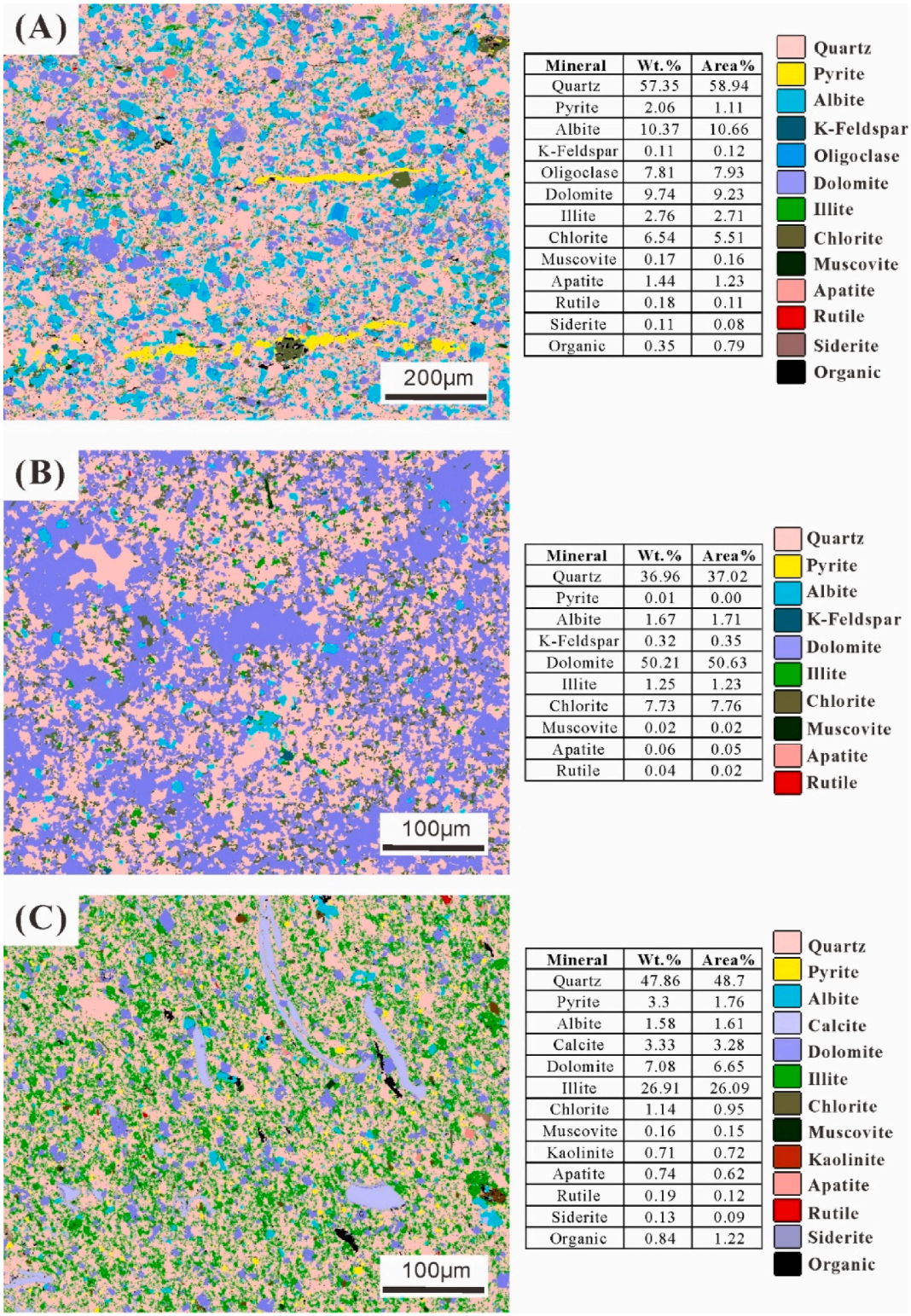

Fig. 3. QEMSCAN mineralogical imaging of representative lithofacies for the Es_4 Member shale samples: (A) Laminated felsic shale (LFS) at a depth of 3225 m; (B) Massive dolomitic mudstone (MDM) at 3248 m; and (C) Laminated mixed shale (MS) at 3280 m.

3.2. Geochemical characteristics

Comprehensive Rock-Eval pyrolysis of 338 core samples from the Es_4 Member reveals significant heterogeneity in both organic matter abundance and hydrocarbon generation potential. Total organic carbon (TOC) values range from 0.10 % to 12.73 %, with an average of 2.72 %, reflecting localized zones of organic enrichment. Free hydrocarbons (S_1) range from 0.01 to 31.91 mg/g rock (avg. 2.62 mg/g rock), while remaining generative potential (S_2) spans from 0.01 to 95.65 mg/g rock (avg. 18.71 mg/g rock). The total hydrocarbon generation potential (PG $= S_1 + S_2$) varies widely from 0.03 to 121.22 mg/g rock, with an average of 21.51 mg/g rock. These broad ranges underscore the variability in

source rock quality across the formation, with several zones showing excellent generative capacity (full dataset provided in the supplementary materials).

Facies-specific geochemical analysis reveals clear differences in generative quality among lithofacies (Fig. 4). Lithofacies LFS exhibits the most favorable source rock attributes, with average values of TOC at 3.71 %, S_1 at 3.76 mg/g rock, S_2 at 25.54 mg/g rock, PG at 29.93 mg/g rock, and extractable organic matter (EOM) at 8.23 mg/g rock. Lithofacies MS also shows strong generative potential, averaging 3.22 % TOC, 2.88 mg/g rock S_1, 22.62 mg/g rock S_2, and 25.59 mg/g rock PG, with EOM at 7.44 mg/g rock. In contrast, lithofacies MDM records significantly lower averages for TOC (1.19 %), S_1 (0.91 mg/g rock), S_2 (7.57 mg/g rock), PG (8.52 mg/g rock), and EOM (3.43 mg/g rock). These trends are clearly illustrated in the boxplots of Fig. 4, with LFS and MS showing both higher medians and broader distributions, while MDM displays consistently low generative indicators, supporting its interpretation as a reservoir facies.

Microscopic evidence further supports this interpretation (Fig. 5). Under cross-polarized and fluorescence light, samples from LFS and MS (panels A–C, G–I) reveal finely dispersed algal organic matter and yellow fluorescent amorphous bitumen, typical of Type I kerogen. Conversely, MDM samples (D, E) show scattered organic particles with weak fluorescence, often associated with microfractures, indicating low-quality, potentially migrabitumen. These petrographic observations corroborate the geochemical findings and emphasize lithofacies-controlled kerogen distribution.

The Hydrogen Index (HI = S_2/TOC × 100) provides critical insight into kerogen type and oil-proneness. According to Lafargue et al. (1998) classification, HI > 600 mg HC/g TOC corresponds to oil-prone Type I kerogen, 300–600 to Type II, and <300 to gas-prone Type III. In the Es_4 Member, LFS and MS are dominated by Type I kerogen, with average HI values of 684 and 689 mg HC/g TOC, respectively. LFS ranges from 123 to 991 mg HC/g TOC, and MS from 1 to 1016 mg HC/g TOC—suggesting strong oil potential but also some heterogeneity in MS. MDM exhibits a wider HI range (36–1077 mg HC/g TOC), but its average HI of 443 mg HC/g TOC indicates a dominance of Type II kerogen, with occasional contributions from lower-quality Type III or inert organic matter. These trends affirm LFS and MS as key source rocks, while MDM represents a less consistent and lower-quality source.

Thermal maturity is evaluated using T_{max}, the temperature at which maximum hydrocarbon generation occurs during pyrolysis. Lithofacies LFS and MS exhibit average T_{max} values of 466 °C and 465 °C, respectively, with most samples falling within the 450–470 °C range, indicative of peak oil generation. Lithofacies MDM, in contrast, shows a broader T_{max} range (351–488 °C) and a lower average of 441 °C. Many MDM samples fall below the oil window threshold (<435 °C), which would imply immaturity. However, this is likely a misrepresentation caused by migrated hydrocarbons. Heavy oils retained in MDM's carbonate-rich matrix can suppress T_{max} by generating early pyrolysis peaks, simulating immaturity. Given MDM's low TOC and HI, these low T_{max} values are better interpreted as artifacts of migrated oil rather than indicators of immature kerogen.

Vitrinite reflectance (R_o) measurements from six shale samples yield values ranging from 0.57 % to 0.64 %, with an average of 0.60 %. However, these values appear significantly lower than the thermal maturity suggested by T_{max}. Using the empirical correlation proposed by Jarvie (2012), R_o (%) = 0.0180 × T_{max} − 7.16, which is widely applied to organic-rich, Type II kerogen within the 435–465 °C range, a T_{max} of 440 °C corresponds to an R_o of ~0.79 %, while 445 °C corresponds to ~0.88 %. For the studied samples with T_{max} reaching 465 °C, the predicted R_o would be around 1.2 %, indicating a substantial discrepancy that warrants further calibration.

This discrepancy may be attributed to R_o suppression, which varies with kerogen type. According to Li et al. (2021), in samples from the same formation in the Jiyang Depression, Type I organic-rich shales showed the highest suppression (0.29 %–0.39 %, avg. 0.32 %), followed by Type II_1 (0.15 %–0.29 %, avg. 0.21 %) and Type II_2 (0.08 %–0.16 %, avg. 0.12 %). In contrast, Type III shales displayed negligible suppression, with measured R_o values closely aligning with equivalent vitrinite reflectance ($EqVR_o$), thus reliably reflecting true maturity. Given the likely presence of Type I to II_1 kerogen in the studied samples, the low measured R_o values may underestimate the actual maturity level.

The oil saturation index (OSI = S_1/TOC × 100) serves as an additional parameter for evaluating hydrocarbon retention. LFS records the highest average OSI (95 mg HC/g TOC), followed by MS (78) and MDM (75). Though OSI values are generally below the 100 mg HC/g TOC crossover threshold (Jarvie, 2012), likely due to evaporative loss and underestimation of S_1, the trend is consistent with facies distribution. High OSI and HI in lithofacies LFS and MS correspond to source-rich intervals, while lithofacies MDM's lower OSI values reflect its reservoir-dominated character, despite occasional elevated S_1 values associated with migrated oil.

Fig. 6 integrates stratigraphic, lithological, and geochemical data for the Es_4 Member (3170–3340 m), providing a vertical profile of key intervals. Lithologically, the section includes calcareous and dolomitic mudstones, oil shale, marly shale, and argillaceous siltstone. Lithofacies LFS is concentrated in the upper and lower intervals, while lithofacies MDM dominates the middle. Geochemical curves (TOC, S_1, S_2, PG, EOM, T_{max}, PI, S_1/TOC, HI) align closely with lithological boundaries, illustrating clear facies control on source and reservoir properties. The coupling of organic-rich LFS and MS with organic-lean MDM reflects a vertically integrated self-sourced shale system in the Damintun Sag.

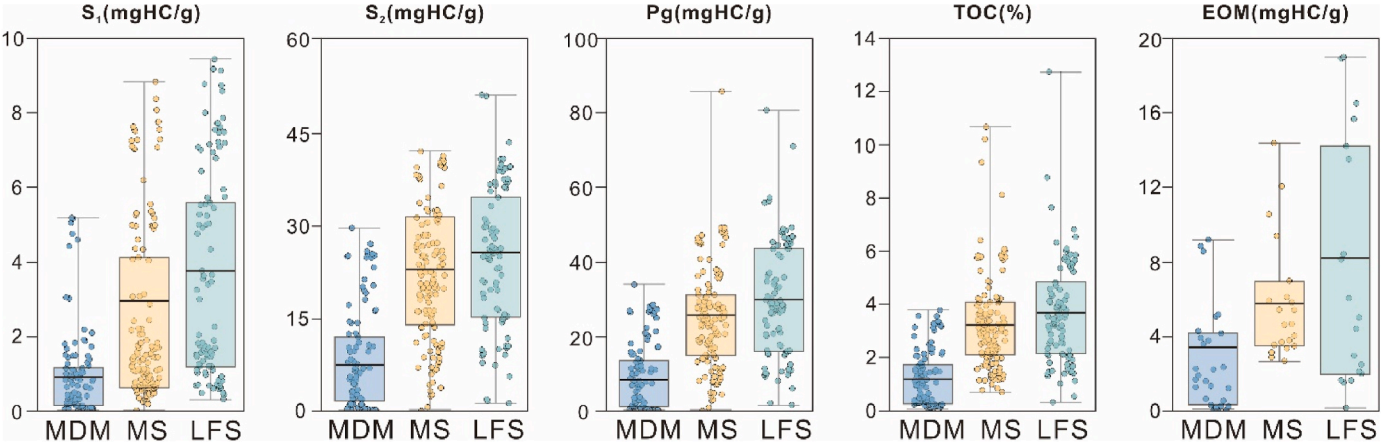

Fig. 4. Box plots showing the distribution of key geochemical parameters for the three lithofacies of LFS, MS, and MDM in the Es_4 Member shale samples.

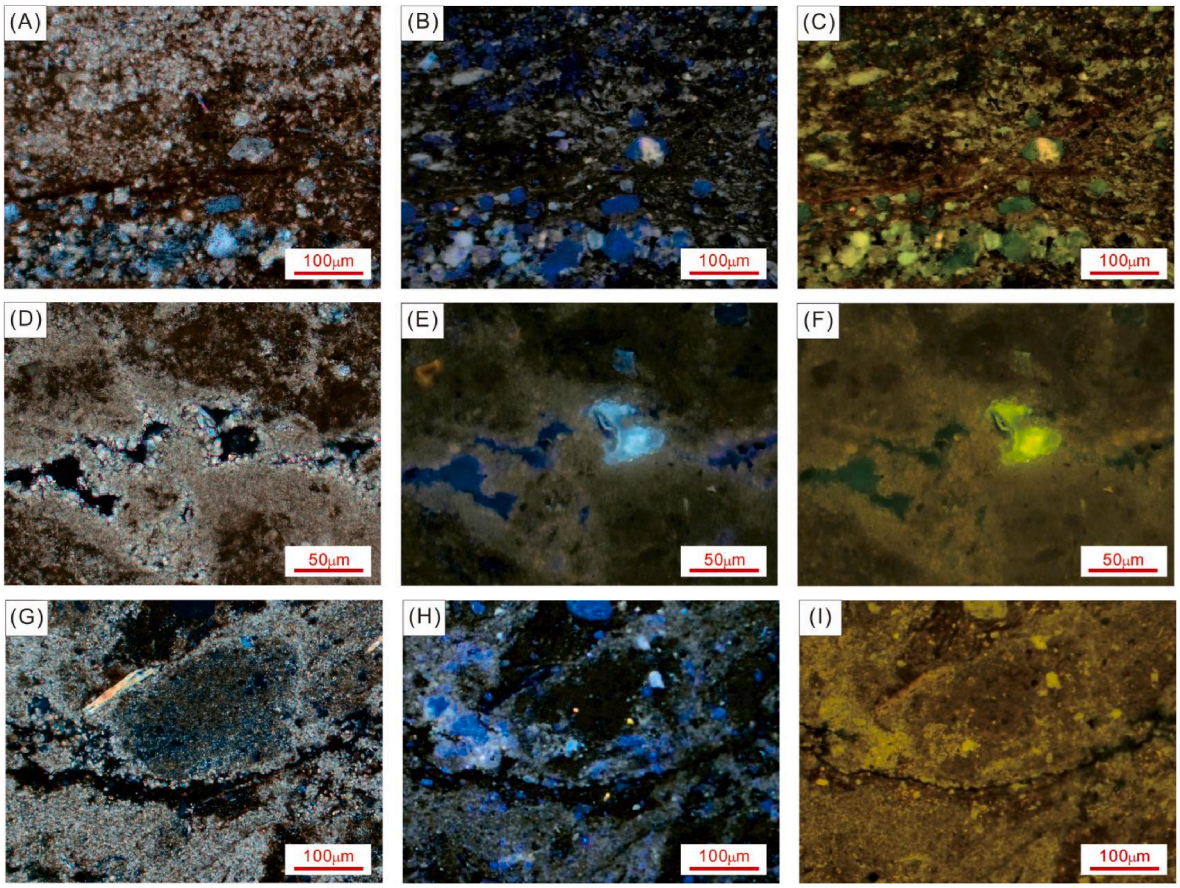

Fig. 5. Optical microscope images showing the occurrence and distribution of organic matter and hydrocarbons in E_{s4} Member shales from the Damintun Sag, images are arranged from right to left under cross-polarized light, violet fluorescence, and blue fluorescence. (A–C) depict laminated felsic shales at 3299 m (Well S352), revealing abundant heavy hydrocarbons (asphaltenes, bitumen) and algal remains, indicative of high organic richness and strong oil-generation potential; (D–F) show massive dolomitic mudstones at 3283.5 m, where free oil is observed within dissolution pores, highlighting their role as reservoirs despite low organic content; and (G–I) illustrate mixed shale at 3279 m, characterized by dispersed organic matter and moderate fluorescence, reflecting intermediate hydrocarbon generation and storage capacity. (For interpretation of the references to color in this figure legend, the reader is referred to the Web version of this article.)

3.3. Pore structure and shale reservoir

Pores in the Es_4 Member occur in a wide range of types and scales, predominantly associated with inorganic mineral constituents. These include intergranular pores between rigid quartz and dolomite grains, intercrystalline pores within lamellar clay aggregates, intraparticle pores in framboidal pyrite, slit-like interlayer pores in clays, and dissolution pores along feldspar grain edges. The majority of these pores range in size from a few nanometers to several hundred nanometers, with typical pore diameters in the 4–30 nm range. FE-SEM imaging (Fig. 7) reveals lithofacies-dependent pore structures. In laminated felsic shale (LFS, 3193 m), bedding-parallel fractures (Fig. 7A), intercrystalline pores in compacted clay aggregates (Fig. 7B), and well-developed pyrite-hosted pores (Fig. 7C) form a continuous, fine-scale network for hydrocarbon storage and migration. In massive dolomitic mudstone (MDM, 3248 m), intergranular pores and organic matter-hosted nanovoids (Fig. 7D), along with dolomite-clay contact pores (Fig. 7E) and intragranular dissolution features in feldspar infilled with illite (Fig. 7F), indicate moderate pore connectivity and localized diagenetic alteration. Mixed shale (MS, 3280 m) presents a combination of both: abundant microfractures, quartz-dolomite intergranular pores (Fig. 7G), organic and feldspar dissolution pores (Fig. 7H), and extensive intergranular dissolution voids along feldspar interfaces (Fig. 7I), reflecting hybrid pore origin through both depositional and post-depositional processes.

FIB-SEM 3D reconstruction offers nanoscale insights into pore shape, volume, and organic associations. In LFS (3223 m; Fig. 8A–C), the pore network is well developed, with complex multimodal distributions comprising both <50 nm nanopores and >100 nm meso-to macropores. These pores often co-occur with organic matter, forming OM-bound porous networks that contribute to both hydrocarbon generation and retention. In MDM (3324 m; Fig. 8D–F), the pore structure is comparatively sparse, and most pores—typically 20–100 nm—are isolated or filled with authigenic minerals or organic residues, suggesting limited connectivity and lower effective porosity. In MS (3233 m; Fig. 8G–I), the pore system includes feldspar-hosted dissolution pores, slit-like interlayer pores, and OM-connected voids ranging from 30 to 300 nm. This lithofacies exhibits moderate connectivity and a broader pore size spectrum, comparable to LFS, but with higher spatial heterogeneity. These differences underscore the controlling influence of mineral composition and diagenesis on nanoscale pore development.

To complement nanoscale observations, MIP experiments (Fig. 9) were employed to evaluate pore size distribution across broader scales. Following IUPAC classification, pores were categorized into micropores (<2 nm), mesopores (2–50 nm), and macropores (>50 nm). In LFS (Fig. 9A), a pronounced mercury uptake peak occurs in the mesopore range (~5–10 nm), with a secondary macropore shoulder at ~10–30 μm, indicating a bimodal distribution conducive to both storage and migration. MDM (Fig. 9B) exhibits similar dual peaks, though with a finer mesopore peak (~4–8 nm) and broader macropore presence (>50 μm), likely associated with feldspar or dolomite dissolution and secondary mineralization. MS (Fig. 9C) is characterized by dominant mesopores in the 6–20 nm range and reduced macropore and micropore

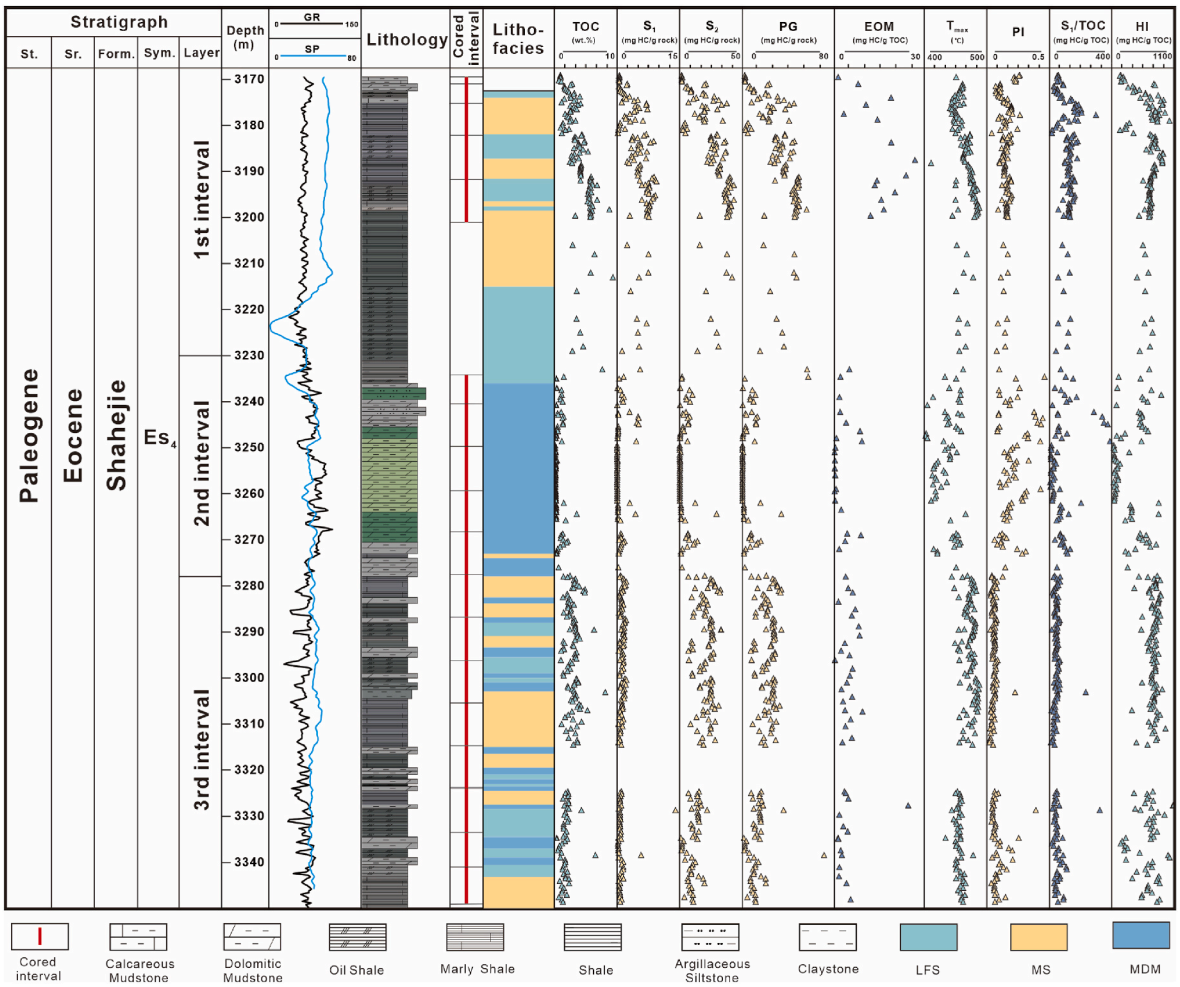

Fig. 6. Integrated stratigraphic profiles showing lithology, lithofacies distribution, and geochemical parameters of the E_{s4} Member shale samples. Core samples, as indicated in the cored interval, were used for experimental analyses, while drilling cuttings were utilized for geochemical and XRD analyses in intervals without core samples.

contributions, reflecting more intensive compaction and less preserved OM-hosted porosity. Mesopores are the largest contributors to total pore volume in all facies, followed by macropores and then micropores. Notably, LFS consistently demonstrates the highest cumulative pore volume and specific surface area, underscoring its superior reservoir potential.

At the micrometer scale, micro-CT scanning and 3D image reconstruction (Fig. 10) reveal the distribution of matrix pores and fracture systems. In LFS (3193.8 m; Fig. 10A–C), matrix pores <10 μm dominate numerically and align along bedding planes, while bedding-parallel fractures exceeding 20 μm in radius contribute significantly to total pore volume and enhance permeability. These fractures, together with rigid mineral-hosted intergranular pores and OM-associated microvoids, establish a highly connected system for fluid flow. In MDM (3265.8 m; Fig. 10D–F), large irregular matrix pores and abundant microfractures – likely induced by hydrocarbon expulsion or overpressure – form secondary conduits that improve lateral flow but remain discontinuous. In MS (3308.6 m; Fig. 10G–I), small matrix pores (<10 μm) are abundant but poorly connected, and fractures are largely absent, resulting in limited permeability. Pore size distribution histograms (Fig. 10C–F, I) further confirm that pores <10 μm account for over 70–85 % of total number, but larger voids and fractures account for a disproportionately high volume, especially in LFS and MDM.

In summary, the Es_4 Member displays a complex, lithofacies-controlled pore system dominated by mineral matrix pores, with substantial variability in pore size, connectivity, and fracture development. LFS emerges as the most favorable lithofacies, with its combination of abundant mesopores, well-connected OM-hosted networks, and extensive bedding-parallel fractures enabling efficient oil storage and short-range migration. MDM exhibits moderate potential, with patchy secondary porosity and microfractures derived from diagenesis and overpressure. MS, while possessing a diverse array of fine-scale pores, suffers from poor connectivity and minimal fracturing, limiting its reservoir performance. This lithofacies-dependent heterogeneity in 3D pore–fracture architecture critically influences reservoir quality, oil accumulation, and producibility. Collectively, the integrated system of nanoscale pores, mesopores, and fractures forms a multi-scale, spatially coupled network that supports effective shale oil development in the Es_4 Member under hydraulic stimulation.

4. Discussion

4.1. Geochemical differentiation of indigenous and migrated hydrocarbons

The identification of indigenous versus migrated hydrocarbons in shale systems such as the Es_4 Member of the Shahejie Formation relies on a comprehensive integration of geochemical and stratigraphic datasets. Rock-Eval pyrolysis parameters, SARA (saturate, aromatic, resin, and asphaltene) composition, and gas chromatographic signatures, when interpreted alongside lithofacies architecture, provide a multidimensional framework to assess hydrocarbon generation, expulsion, and

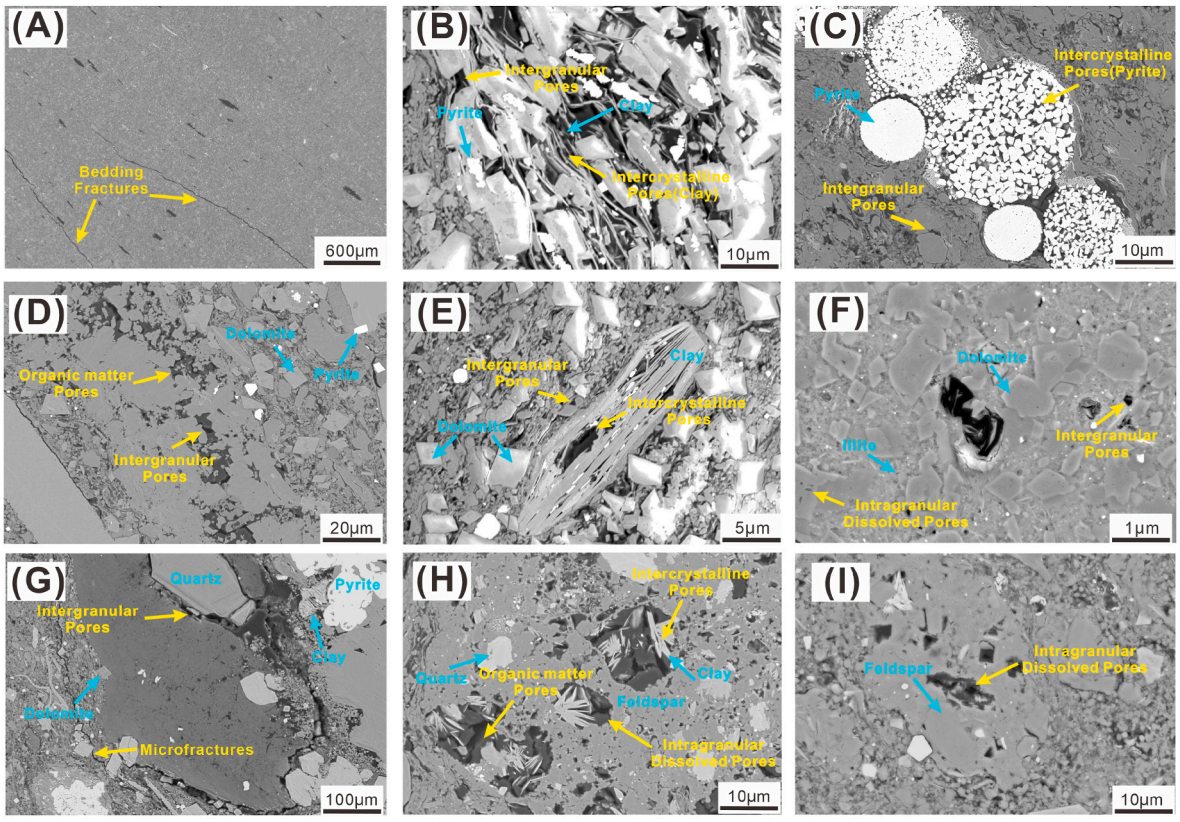

Fig. 7. FE-SEM images illustrating the morphology, types, and mineral associations of pore structures in shales from the Es_4 Member.

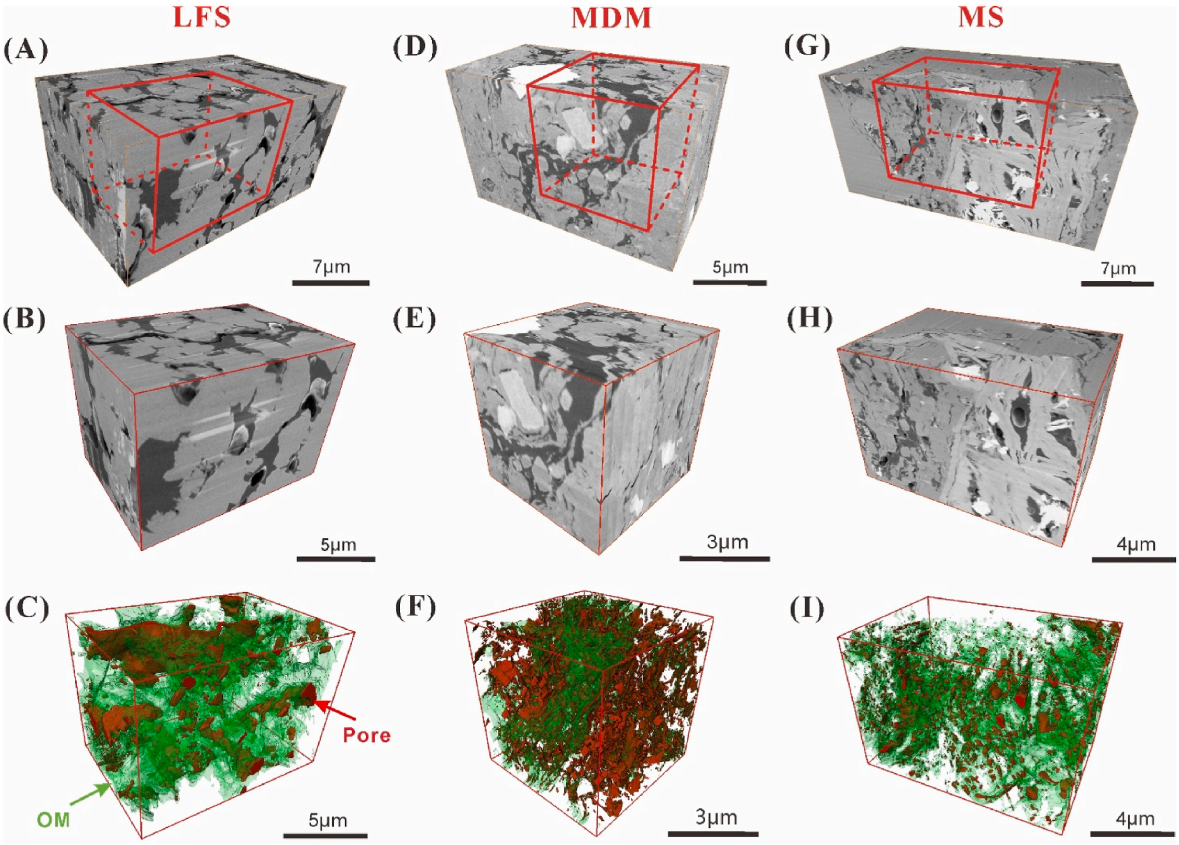

Fig. 8. FIB-SEM images of shale samples from the Es_4 Member. (A–C): Laminated felsic shale at a depth of 3223 m; (D–F): Massive dolomitic mudstone at 3324 m; (G–I): Mixed shale at 3233 m.

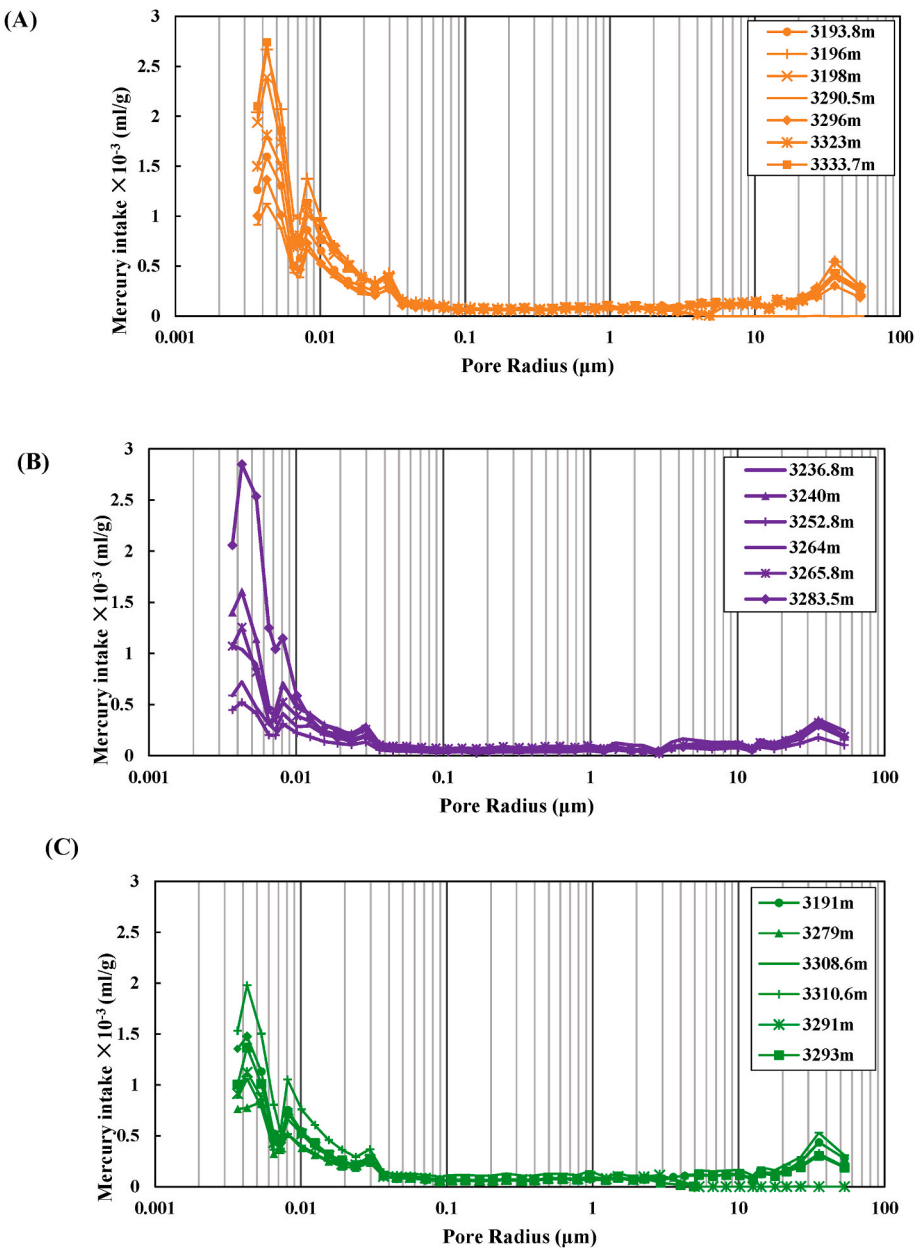

Fig. 9. MIP capillary pressure curves illustrating pore-throat size distributions for different lithofacies within the Es4 Member shale samples: (A) Laminated felsic shale; (B) Massive dolomitic mudstone; (C) Laminated mixed shale.

migration behavior. In the Es_4 Member, source-rich lithologies such as laminated felsic shale (LFS) and mixed shale (MS) are shown to expel hydrocarbons into adjacent, organic-lean intervals such as massive dolomitic mudstone (MDM), resulting in a distinct geochemical zoning that reflects short-distance, stratigraphically controlled migration (Han et al., 2015; Ji et al., 2024).

Rock-Eval cross-plots are particularly effective in distinguishing between in-situ and migrated oils. In the S_1/TOC vs. T_{max} diagram (Fig. 11A), most LFS and MS samples exhibit S_1/TOC values below 100 mg HC/g TOC and T_{max} values above 440 °C—signatures of indigenous hydrocarbons that remain associated with the host kerogen. In contrast, samples with anomalously high S_1/TOC (>100 mg HC/g TOC) and suppressed T_{max} (<440 °C), typically occurring in MDM layers, indicate migrated hydrocarbons. These intervals often coincide with stratigraphic contacts where overlying MDM units receive expelled oil from underlying LFS/MS beds. The suppression of T_{max} and enrichment in free hydrocarbons are classic indicators of secondary hydrocarbon input (Jarvie, 2012; Katz and Lin, 2021) (see Fig. 12).

Further insights are provided by Tmax vs. TOC relationships (Fig. 11B), which define two distinct maturity regimes. Samples with TOC below 2 %—mostly from MDM—show variable and often low Tmax values due to dilution and suppression effects from migrated oils. In contrast, samples from LFS and MS with TOC above 2 % exhibit consistent Tmax values over 440 °C, signifying localized hydrocarbon generation without external influence. These data indicate that MDM acts as a secondary reservoir receiving hydrocarbons from adjacent organic-rich layers, with stratigraphic proximity playing a decisive role in migration efficiency.

The Production Index (PI) serves as another critical proxy. In the PI vs. TOC cross-plot (Fig. 11C), MDM samples often exhibit high PI values despite low TOC, pointing to oil charging from an external source. LFS and MS samples with high TOC show a spectrum of PI values: moderate PI where hydrocarbons are retained, and low PI where expulsion has already occurred. This inverse relationship between PI and TOC helps

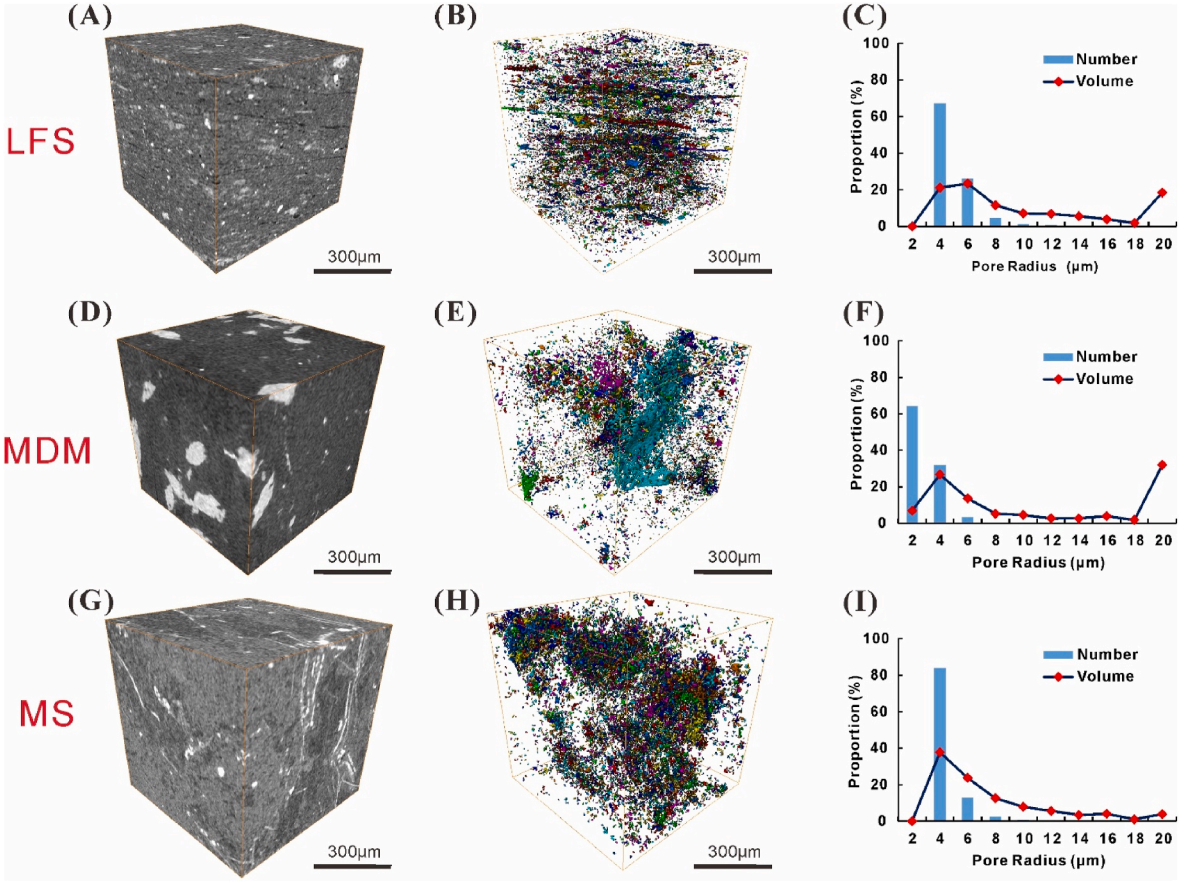

Fig. 10. Micro-CT scan images and corresponding 3D pore structure models of representative lithofacies from Es_4 Member shale samples: (A–C) Laminated felsic shale (3193.8 m), (D–F) Massive dolomitic mudstone (3265.8 m), and (G–I) Laminated mixed shale (3308.6 m).

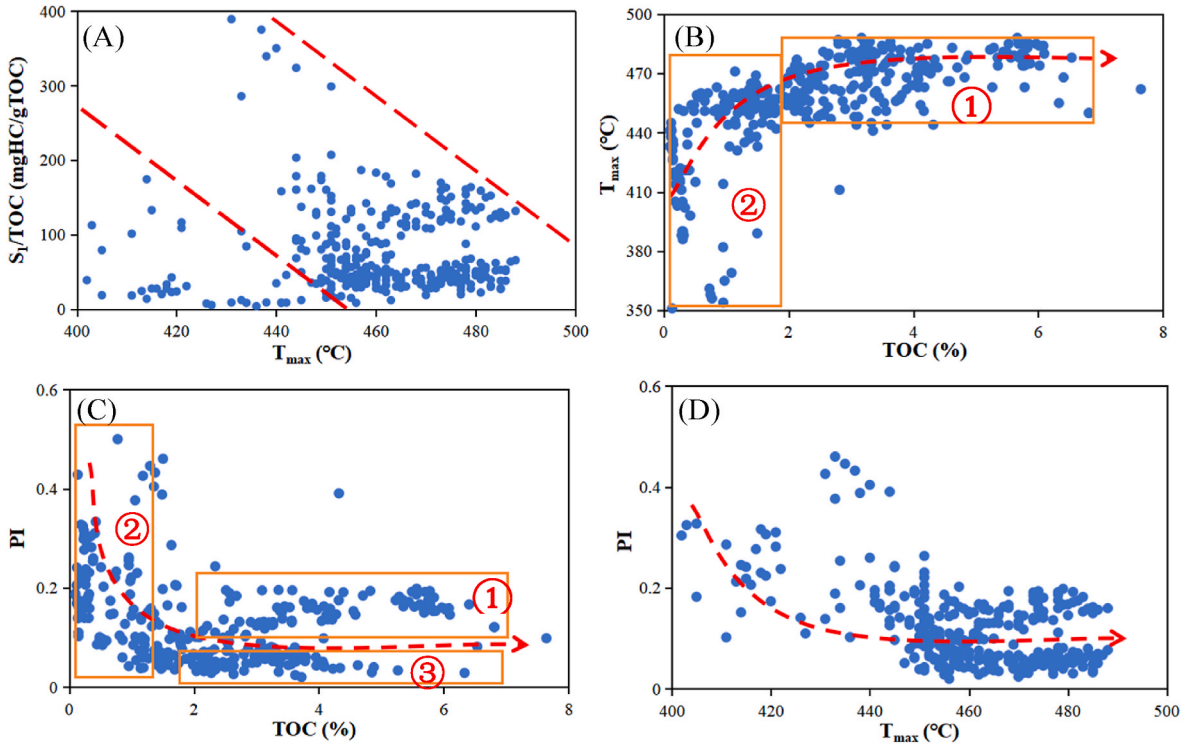

Fig. 11. Crossplots of Rock-Eval pyrolysis parameters and TOC for shale samples from the Es_4 Member: (A) Crossplot of S_1/TOC vs. T_{max}; (B) Crossplot of T_{max} vs. TOC content; (C) Crossplot of Production Index (PI) vs. TOC; (D) Plot of PI vs. T_{max}.

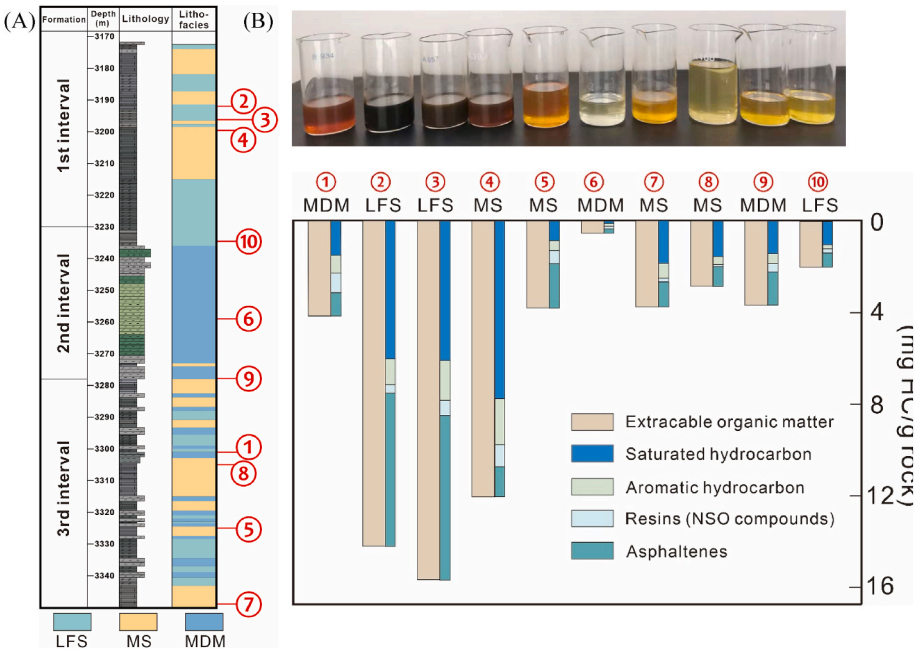

Fig. 12. Extractable organic matter (EOM) content (B) of shale core samples from various depths and lithofacies within the Es_4 Member (A). The numbering order ① to ⑩ in (B) is based on the color gradient of the EOM. (For interpretation of the references to color in this figure legend, the reader is referred to the Web version of this article.)

identify zones of active generation, expulsion, and migration. Similarly, in the PI vs. T_{max} plot (Fig. 11D), elevated PI values at $T_{max} < 430$ °C correspond to migrated oils, while $T_{max} > 440$ °C with lower PI confirms indigenous maturation. Together, these patterns highlight T_{max} suppression and PI elevation as robust markers of migrated hydrocarbon enrichment (Peters, 1986).

The lithological and geochemical framework presented in Fig. 6 spatially contextualizes these findings. LFS and MS intervals consistently show high TOC, elevated S_2, and stable T_{max} values, marking them as primary source rocks. Meanwhile, adjacent MDM units, despite low TOC, display high S_1/TOC, OSI, and extractable organic matter (EOM), particularly where they directly contact source-rich beds. These patterns reflect selective short-distance vertical migration. Conversely, intervals dominated by claystone or argillaceous siltstone, which lack such geochemical enrichments, act as intraformational seals that inhibit further migration, reinforcing a bed-scale coupling model (Fig. 12).

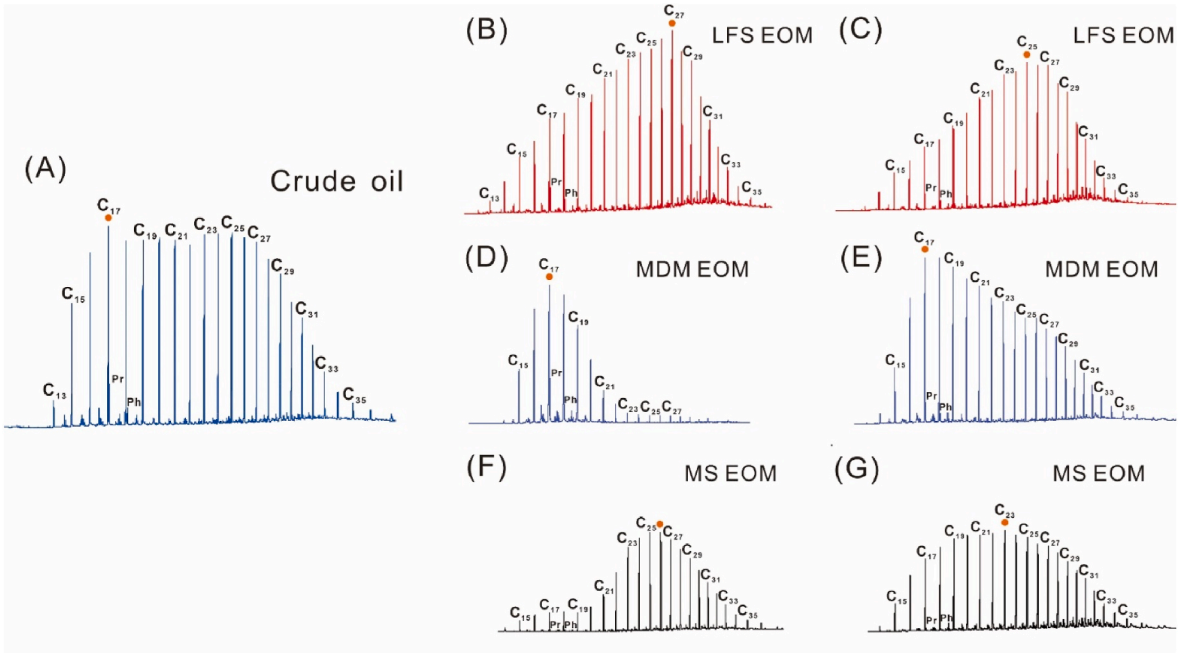

Fig. 13. Gas chromatograms of saturated hydrocarbons from crude oil and extractable organic matter (EOM) across three lithofacies in Well S352, Es_4 Member shale samples: (A) Crude oil from Well S352; (B–C) Laminated feldspathic shale at 3192 m and 3196.2 m; (D–E) Massive dolomitic mudstone at 3259 m and 3301 m; (F–G) Mixed shale at 3305 m and 3348.9 m. Orange circles highlight the main carbon peaks in each chromatogram. (For interpretation of the references to color in this figure legend, the reader is referred to the Web version of this article.)

This localized migration is further substantiated by molecular-level evidence from gas chromatography. The reference crude oil chromatogram of saturtaed hydrocarbon fraction (Fig. 13A) displays a full-range *n*-alkane distribution (C_{13}–C_{35}) with a Gaussian-shaped peak at C_{23}–C_{25} and balanced pristane/phytane (Pr/Ph) ratios—features typical of mature, unaltered oil. Lithofacies LFS samples (Fig. 13B and C) show similar full-spectrum chromatograms, with peaks shifted slightly heavier (C_{27}–C_{29}), confirming their role as source facies where heavier hydrocarbons are retained due to minimal migration and strong kerogen adsorption (Leythaeuser et al., 1984).

In contrast, lithofacies MDM samples (Fig. 13D and E) exhibit truncated chromatograms dominated by light *n*-alkanes (C_{15}–C_{21}) and depleted heavy components beyond C_{27}. These profiles signify that only light, mobile hydrocarbons reached these intervals, consistent with secondary migration and geochromatographic fractionation. The distinct peak at C_{17} and loss of higher molecular weight compounds confirm MDM as a passive recipient of migrated oils. Lithofacies MS samples (Fig. 13F and G) exhibit intermediate chromatograms, with broad distributions peaking between C_{23} and C_{27} and moderate loss of light and heavy ends, suggesting partial in-situ generation and some contribution from adjacent migration.

The systematic shift in *n*-alkane peak positions across facies from C_{25}–C_{27} in LFS, to C_{23}–C_{25} in MS, and C_{17}–C_{19} in MDM, mirrors the expected outcome of compositional fractionation during expulsion and migration. This pattern, driven by differences in molecular weight, mobility, and adsorption capacity, underscores the physical and chemical selectivity of migration processes in fine-grained systems (Raji et al., 2015). It also validates the spatial model proposed from pyrolysis data, whereby LFS acts as the dominant source, MS plays a transitional role, and MDM functions as the primary migration endpoint.

In summary, the combined use of Rock-Eval pyrolysis (S_1, S_2, T_{max}, PI, OSI), lithofacies analysis, and gas chromatography provides a comprehensive framework to distinguish indigenous hydrocarbons from migrated oils in the Es_4 Member. Migrated hydrocarbons are typified by high S_1/TOC, high PI, low TOC, suppressed T_{max}, and truncated chromatograms dominated by light alkanes—mainly found in MDM. Indigenous hydrocarbons, by contrast, show high TOC and S_2, stable T_{max}, moderate PI, and balanced n-alkane profiles with heavy-end retention—primarily occurring in LFS and MS. These integrated indicators not only reveal spatial and chemical pathways of hydrocarbon transfer but also enhance the resolution of sweet spot prediction in lacustrine shale oil systems.

4.2. Conceptual model of lithofacies-controlled shale oil expulsion and migration

Understanding the mechanisms controlling hydrocarbon enrichment in shale oil systems—especially under low-maturity conditions—is essential for identifying productive zones and optimizing exploration targets (Zou et al., 2019). In the Es_4 Member, the vertical alternation of organic-rich LFS and MS with organic-lean MDM creates a tightly coupled source–reservoir sequence. This stratigraphic arrangement promotes localized, bed-scale hydrocarbon migration and storage, consistent with the short-distance enrichment patterns observed in other lacustrine basins (Hu et al., 2022; Ji et al., 2024). These lithological transitions are accompanied by microstructural heterogeneity and evolving pore networks, which control the timing, efficiency, and direction of oil movement.

A three-stage conceptual model (Fig. 14) is proposed to describe the microscale processes driving shale oil expulsion and migration. In Stage 1, hydrocarbons are initially generated within the LFS and MS lithofacies at early stages of thermal maturation. Here, generated oil is strongly adsorbed onto kerogen surfaces and partially absorbed by swelling organic matter. This oil is retained within nanometer-scale pores until kerogen saturation is reached (Zhang et al., 2019). Once the volume of generated hydrocarbons exceeds the volume of organic pore spaces, internal pore pressure increases, initiating migration into nearby inorganic pores—such as interlayer clay pores and framboidal pyrite-associated voids. These early migration steps are molecularly selective, with heavy hydrocarbons remaining trapped while lighter compounds are gradually redistributed within the mineral matrix (Krooss et al., 1991).

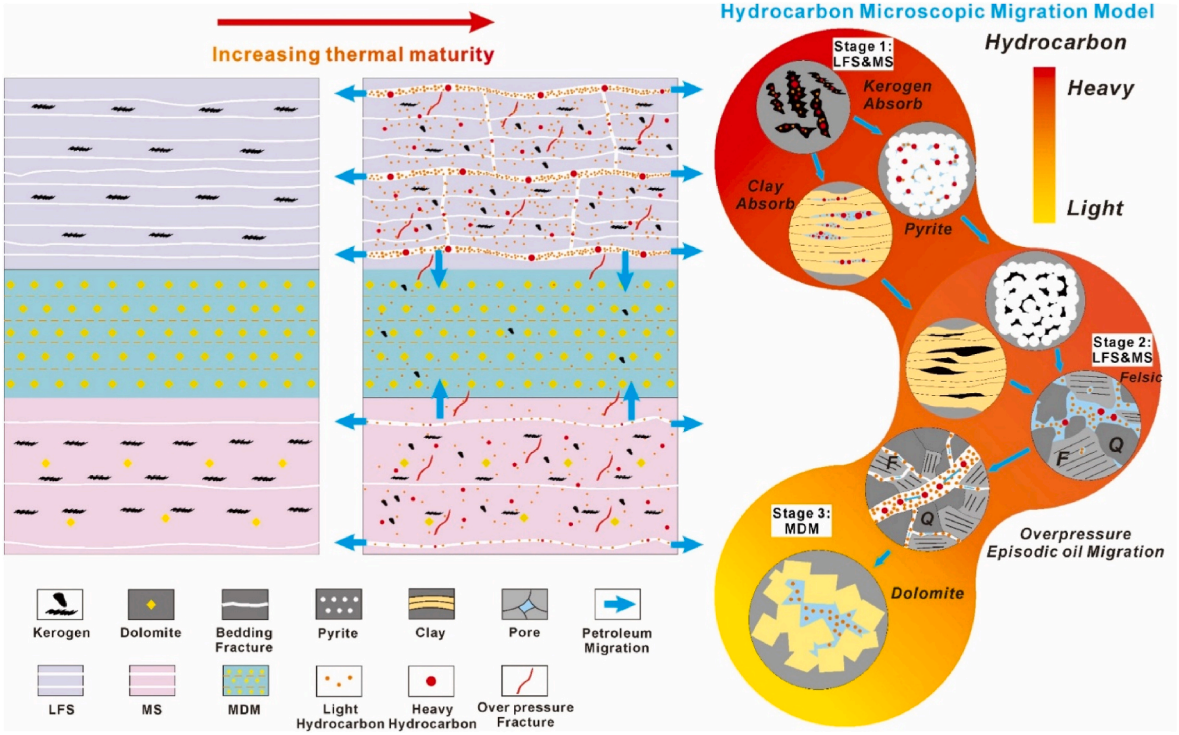

Fig. 14. A conceptual model of hydrocarbon expulsion and migration in the Es_4 Member shale samples based on data from Well S352.

With continued oil generation, Stage 2 is characterized by the development of overpressure and broader-scale lateral migration. As pore fluid pressure rises, it eventually exceeds the capillary entry pressure of surrounding minerals, enabling hydrocarbon movement through connected micro- and meso-pore networks. Migration at this stage is primarily confined to bedding-parallel planes within LFS and MS, where the presence of laminated structures enhances horizontal conductivity. Bedding fractures, fissile planes, and aligned mineral grains form low-resistance pathways for oil migration, particularly in clay-rich or finely layered intervals. These structural conduits allow significant lateral transport of lighter oil components into adjacent intervals, especially along lithological boundaries (Ji et al., 2024).

Once pore pressure surpasses the mechanical integrity of the rock matrix, Stage 3 begins. This stage involves overpressure-induced fracturing, often in vertical orientations, which connect with preexisting horizontal fractures to establish three-dimensional migration networks (Kalani et al., 2015; Teixeira et al., 2017). These fracture systems substantially increase the effective permeability of the shale, providing escape routes for oil generated at depth. Vertical migration is particularly important for transferring hydrocarbons from LFS/MS into the overlying or underlying MDM, which serves as the principal storage unit despite its poor generative capacity. The episodic nature of this fracture-driven expulsion may lead to pulsating migration events, further contributing to compositional heterogeneity in the accumulated oil.

As oil moves from source-rich to reservoir-prone facies, geochromatographic fractionation plays a central role in controlling compositional changes. Heavy hydrocarbons, due to their larger molecular size and lower mobility, tend to remain adsorbed in source rock or accumulate near the expulsion front, while light hydrocarbons migrate farther, resulting in an enrichment gradient (Raji et al., 2015; Ji et al., 2024). This phenomenon is evident in the GC chromatograms and SARA data from Well S352, where MDM intervals show elevated levels of lighter components, indicating short-distance charging from adjacent LFS/MS. The microscale absorption patterns shown in Fig. 14—kerogen, clay, and pyrite surfaces preferentially interacting with heavy hydrocarbons—highlight how mineralogy mediates hydrocarbon movement at each migration stage.

The model also underscores the spatial and temporal compartmentalization of hydrocarbon systems in the Es_4 Member. In early stages, oil is confined within kerogen-associated pores. As maturity progresses, migration shifts to connected pore systems and finally to fracture-assisted pathways, allowing selective vertical migration. This evolution helps explain the observed discrepancies in oil composition and saturation between lithofacies: high TOC LFS/MS layers contain indigenous, heavier oil signatures, while low-TOC MDM layers show evidence of light, migrated oil—despite lacking intrinsic generative capacity. The limited vertical connectivity outside of induced fractures confirms that large-scale, basin-wide migration is unlikely in this low-maturity system.

The conceptual model derived from Fig. 14 and core analyses from Well S352 reveals that oil expulsion and migration in the Es_4 Member operate through a phased, lithofacies-controlled process. Hydrocarbons are initially generated and retained within kerogen and mineral surfaces, then laterally transported through lamination-enhanced pathways, and eventually vertically expelled into dolomitic reservoirs via fracture networks. Each stage is governed by mineral-pore interactions, pressure buildup, and lithofacies architecture, producing highly localized migration and compositional fractionation. These insights are critical for delineating sweet spots and improving predictive models for shale oil development in similar lacustrine settings.

4.3. Integrated controls on sweet spot prediction

Sweet spot prediction in the Es_4 shale of the Damintun Sag relies on the integration of geological, geochemical, and petrophysical parameters. Characterized by low to moderate maturity and strong lithological heterogeneity, the Es_4 Member provides a favorable setting for localized shale oil enrichment. Understanding how source rock quality, pore structure, hydrocarbon migration, thermal maturity, and fracture development interact is essential for delineating productive zones.

Although measured R_o in the studied samples averages around 0.60 %, a high proportion of free oil is observed, suggesting effective hydrocarbon generation and retention even at seemingly immature levels. This discrepancy may be attributed to R_o suppression, a known phenomenon in organic-rich, algal-dominated Type I kerogen. Li et al. (2021) reported suppression of up to 0.39 % in similar kerogen types from the Jiyang Depression, implying actual maturity may fall within the effective oil window. Free oil, residing in larger pores and fractures, is critical for production due to its higher mobility relative to adsorbed oil (Li et al., 2022; Zhang et al., 2022).

In addition, organic matter-hosted pores remain underdeveloped, lithofacies LFS and MS still show abundant intergranular, intercrystalline, and mineral-hosted nanopores at ~0.6 % R_o. Maturity-related feldspar and carbonate dissolution further contribute to secondary porosity beyond the 0.6 % R_o threshold (Mastalerz et al., 2013; Huang et al., 2025).

Source rock quality and geochemical zoning are key to sweet spot identification. Lithofacies LFS and MS serve as primary source lithofacies, featuring high TOC (3.2–3.7 %), elevated HI, and strong generative potential (S_2 and PG), consistent with Type I oil-prone kerogen (Jarvie, 2012; Han et al., 2015; Ma et al., 2025). In contrast, lithofacies MDM has low TOC (<1.5 %) and poor generative capacity but functions effectively as a reservoir. Indicators such as high oil saturation index (OSI; S_1/TOC >100 mg/g) and low T_{max} (<440 °C) signal migrated oil in MDM (Li et al., 2022; Wang et al., 2022), although migration is generally limited to zones near lithofacies boundaries due to low overall maturity.

Hydrocarbon migration and lithofacies coupling play a pivotal role in enrichment. Sweet spots typically form where source-rich LFS/MS directly contact reservoir-prone MDM, enabling short-distance lateral migration of oil. This spatial arrangement increases the chance of accumulation in MDM despite its low TOC. Bedding-parallel fractures along lamina boundaries and overpressure-induced vertical fractures further enhance hydrocarbon expulsion, migration, and storage (Yuan et al., 2019; Gao et al., 2024). This lithological-structural coupling is crucial for localizing productive zones.

Pore structure is another fundamental control on shale reservoir quality. Key attributes such as pore volume, surface area, and pore size distribution, combined with fracture intensity, govern oil storage and flow (Curtis et al., 2012; Yuan et al., 2019). In low-maturity shales, complex micro- and nanopore systems are commonly observed. Though fractures contribute little to total porosity, they are essential pathways for hydrocarbon migration and act as transient storage zones. Horizontal bedding fractures often form along mechanically weak lamina and are intensified by overpressure from organic matter decomposition (Wang et al., 2024). SEM imagery reveals bitumen aligned along fractures and within intergranular pores in quartz and dolomite, confirming their active role in hydrocarbon transport and retention.

A robust sweet spot prediction model integrates these geological and geochemical indicators—TOC, S_1, S_2, HI, T_{max}, PI, pore structure type, fracture development, and lithofacies architecture. Coupling these with migration markers like S_1/TOC ratios and GC fingerprints enhances sweet spot delineation accuracy, offering guidance for horizontal well planning and pilot production in the Es_4 shale.

Based on mercury intrusion, SEM, and 3D pore network reconstruction, Es_4 reservoirs are categorized into three types: Type I (LFS), with abundant interbedded fractures and high oil mobility; Type II (MS), with moderate properties; and Type III (MDM), with limited fractures and poor flow capacity. Sweet spots are typically associated with Type I and II reservoirs. In Well S352, the most productive interval lies at

3180–3200 m, where thick, organic-rich LFS and MS layers generate oil, develop overpressure, and contain well-developed fractures. A secondary target occurs near 3240 m in the MDM interval, which has received migrated oil from adjacent LFS. While MDM may be more favorable in higher maturity systems, its limited fracture development currently poses engineering challenges, despite its high OSI indicating significant oil saturation.

4.4. Global comparison and implications for low-maturity shale oil systems

Recent exploration successes have demonstrated that low-maturity shale oil systems can be commercially viable when hydrocarbon generation, retention, and migration are effectively coupled with favorable lithofacies and pore network architectures. The Es_4 Member in the Damintun Sag presents a representative example of such a system, characterized by Type I kerogen, laminated source rocks, and stratigraphic confinement that supports oil enrichment even at suppressed vitrinite reflectance values (~0.60 %). To contextualize the broader significance of this case, comparative insights from global low-maturity shales are instructive.

The Upper Carboniferous–Permian succession in the Zaysan Basin (Kazakhstan) offers a close analogue. Nurbekova et al. (2023) documented high TOC values (>5.0 wt%), low R_o values (<0.65 %), and oil-prone Type II/III kerogen, with extractable bitumen yields indicating excellent hydrocarbon potential despite low maturity. These features mirror the geochemical behavior observed in the Es_4 Member, particularly in LFS and MS lithofacies, where TOC values exceed 3.0 wt% and hydrogen indices point to highly oil-prone kerogen. Importantly, both systems exhibit suppressed maturity markers yet retain significant *in situ* oil, emphasizing the need to reassess conventional maturity cutoffs in such systems.

In the Eagle Ford Formation (USA), similar patterns have been recognized, where early-mature source rocks with moderate R_o values (~0.6–0.8 %) still produce substantial oil volumes due to high organic content and favorable pore systems (Jarvie, 2012; Hackley and Cardott, 2016). Likewise, in the lacustrine Green River Formation, Johnson et al. (2016) reported that oil generation and expulsion occurred at low maturity, aided by lamination, fine-grained sedimentation, and localized overpressure. These factors allowed hydrocarbons to migrate into nearby carbonate-rich beds with diagenetically enhanced porosity—closely resembling the Es_4's interplay between LFS/MS source intervals and MDM reservoir beds.

Regionally, both the Shahejie Formation in the Jiyang Depression and the Nenjiang Formation in the Songliao Basin provide compelling analogues to the Es_4 Member. In the Shahejie Formation, Liu et al. (2023) identified Tmax–Ro suppression linked to Type I algal kerogen and demonstrated that localized hydrocarbon migration could be traced through gas chromatography (GC) fingerprints and anomalously high S_1/TOC ratios—patterns that align closely with those observed in the Es_4 Member, where thermal suppression, extractable organic matter (EOM) enrichment, and elevated S_1 values in carbonate-rich MDM layers indicate stratigraphically confined, short-range oil migration. Similarly, in the Nenjiang Formation, He et al. (2024) reported low-maturity, laminated source rocks coupled with adjacent carbonate reservoirs and effective intraformational seals—mirroring the lithofacies-controlled enrichment model established for the Es_4 system.

Across these low-maturity shale systems, a consistent theme emerges: geological factors such as fine lamination, high TOC, oil-prone kerogen types, and favorable lithofacies juxtapositions frequently play a more decisive role in hydrocarbon enrichment than thermal maturity alone. Effectively identifying sweet spots under these conditions requires an integrated methodology. What sets the present study apart is its comprehensive, multidisciplinary workflow that combines core-based lithofacies classification, high-resolution geochemical fingerprinting (including Rock-Eval pyrolysis, gas chromatography, and extractable organic matter analysis), calibrated thermal maturity assessments, and multiscale pore network imaging techniques such as FE-SEM, FIB-SEM, MIP, and micro-CT scanning.

This integrated approach captures not only generative potential but also oil retention and migration capacity—critical for evaluating enrichment under low-maturity conditions. It provides a transferable template for assessing other low-maturity or frontier basins, especially where traditional maturity thresholds may underestimate resource potential.

In particular, diagnostic tools such as S_1/TOC vs. T_{max} crossplots, PI vs. TOC anomalies, GC-based *n*-alkane fractionation, and spatial EOM patterns are powerful indicators of migrated versus indigenous hydrocarbons. Their application, when tied to lithofacies architecture and pore–fracture system analysis, enhances sweet spot predictability.

5. Conclusions

This study presents a multidisciplinary assessment of sweet spot prediction in the Es_4 Member of the Damintun Sag by integrating lithofacies, geochemistry, pore structure, and hydrocarbon migration characteristics. The results confirm that productive intervals are closely associated with the coupling of source-rich laminated felsic shale (LFS) and mixed shale (MS) with adjacent, reservoir-prone massive dolomitic mudstone (MDM). LFS and MS lithofacies exhibit high TOC, strong generative potential, and favorable pore systems, including mesopores, organic matter-hosted pores, and bedding-parallel fractures, which facilitate efficient oil generation, retention, and short-range migration.

Despite low measured R_o values (~0.6 %), T_{max} data and geochemical indicators suggest that actual thermal maturity is higher, potentially due to suppression from Type I algal kerogen. This underlines the importance of integrating multiple maturity proxies in low-maturity shale systems. MDM, although a poor source rock, serves as an effective migration endpoint, especially when in close contact with LFS/MS. Its occasional enrichment in light hydrocarbons, supported by high OSI and truncated GC profiles, reflects localized, stratigraphically confined oil charging.

Advanced pore characterization using SEM, FIB-SEM, MIP, and micro-CT imaging confirms that lithofacies control pore geometry, connectivity, and ultimately reservoir performance. LFS consistently demonstrates the most favorable pore–fracture network, making it a prime exploration target (Type I reservoir), followed by MS (Type II). MDM (Type III), although less connected, may still be viable under higher maturity conditions or with hydraulic stimulation.

The proposed conceptual model linking lithofacies architecture, pore systems, geochemical zonation, and migration pathways provides a predictive framework for sweet spot identification in low-maturity lacustrine shale systems. The findings offer broader implications for global analogues, such as the Eagle Ford, Green River, Shahejie, Nenjiang, and Zaysan formations, and highlight the importance of moving beyond conventional maturity screening by focusing on depositional facies, organic preservation, pore–fracture development, and short-range oil migration.

CRediT authorship contribution statement

Yong Ma: Writing – review & editing, Writing – original draft, Formal analysis, Conceptualization. **Qinhong Hu:** Writing – review & editing, Methodology. **Jianbin Xu:** Writing – review & editing, Methodology, Data curation. **Binhao Feng:** Writing – review & editing, Investigation, Data curation. **Fujie Jiang:** Writing – review & editing, Conceptualization. **Yanshan Wang:** Writing – review & editing, Investigation, Data curation. **Haiping Huang:** Writing – review & editing, Writing – original draft, Conceptualization.

Declaration of competing interest

The authors declare no competing interests.

Acknowledgements

This research was funded by the National Natural Science Foundation of China (Grant Nos. 42173030 and 42473034) and the Open Project from the Key Laboratory of Shale Gas Exploration, Ministry of Natural Resources (KLSGE-202406). We also extend our heartfelt appreciation to Dr. Milovan Fustic from Nazarbayev University and one anonymous reviewer for their valuable comments that significantly enhanced the quality of this manuscript.

Appendix A. Supplementary data

Supplementary data to this article can be found online at https://doi.org/10.1016/j.marpetgeo.2025.107559.

Data availability

Data will be made available on request.

References

Cardott, B.J., 2012. Thermal maturity of Woodford Shale gas and oil plays, Oklahoma, USA. Int. J. Coal Geol. 103, 109–119.
Chen, K., Zhang, J., Tang, X., Huang, X., 2015. Analysis of influence factors for shale oil contents in 4th member of Shahejie Formation in damintun Sag. China pet. Explor 20, 22–28 (In Chinese with English abstract).
Chen, G., Lu, S., Zhang, J., Wang, M., Li, J., Xu, C., Pervukhina, M., Wang, J., 2017. Estimation of enriched shale oil resource potential in E2s4L of Damintun Sag in Bohai Bay Basin, China. Energy Fuels 31, 3635–3642.
Chen, X., Qu, X., Xu, S., Wang, W., Li, S., He, H., Liu, Y., 2020. Dissolution pores in shale and their influence on reservoir quality in Damintun depression, Bohai Bay Basin, East China: insights from SEM images, N2 adsorption and fluid–rock interaction experiments. Mar. Petrol. Geol. 117, 104394.
Curtis, M.E., Cardott, B.J., Sondergeld, C.H., Rai, C.S., 2012. The Development of Organic Porosity in the Woodford Shale Related to Thermal Maturity. SPE–160158.
Drake, W.R., Bazzell, A., Curtis, J., Zumberge, J., 2019. Variability in Oil Generation and Migration with Thermal Maturity: Wolfcamp and Spraberry Formations. Northern Midland Basin, Texas. URTEC 461.
Gao, Z., Bai, L., Hu, Q., Yang, Z., Jiang, Z., Wang, Z., Xin, H., Zhang, L., Yang, A., Jia, L., Liu, Z., Ma, G., 2024. Shale oil migration across multiple scales: a review of characterization methods and different patterns. Earth Sci. Rev. 254, 104819.
Guo, P., Yao, L., Ren, D., 2016. Simulation of three–dimensional tectonic stress fields and quantitative prediction of tectonic fracture within the Damintun depression, Liaohe Basin, northeast China. J. Struct. Geol. 86, 211–223.
Hackley, P.C., Cardott, B.J., 2016. Application of organic petrography in North American shale petroleum systems: a review. Int. J. Coal Geol. 163, 8–51.
Han, Y., Mahlstedt, N., Horsfield, B., 2015. The Barnett Shale: compositional fractionation associated with intraformational petroleum migration, retention, and expulsion. AAPG Bull. 99, 2173–2202.
Hao, F., Zou, H., Li, X., Jiang, J., 2009. Migration and occurrence of high wax oils in the Damintun depression, Northeast, China: implication for primary controls of petroleum migration pathways in heterogeneous carrier beds. J. Pet. Sci. Eng. 67, 105–115.
He, W., Cui, B., Zhang, J., Zhao, Y., Cheng, X., Liu, Z., Liu, X., Zeng, H., 2024. Geological characteristics and exploration breakthroughs of the middle to low mature shale oil of Nenjiang Formation in northern Songliao Basin. Acta Pet. Sinica 45, 900–913 (In Chinese with English Abstract).
Hou, L., Yu, Z., Luo, X., Lin, S., Zhao, Z., Yang, Z., Wu, S., Cui, J., Zhang, L., 2021. Key geological factors controlling the estimated ultimate recovery of shale oil and gas: a case study of the Eagle Ford shale, Gulf Coast Basin, USA. Pet. Explor. Develop. 48, 762–774.
Hu, S., Bai, B., Tao, S., Bian, C., Zhang, T., Chen, Y., Liang, X., Wang, L., Zhu, R., Jia, J., Pan, Z., Li, S., Liu, Y., 2022. Heterogeneous geological conditions and differential enrichment of medium and high maturity continental shale oil in China. Pet. Explor. Development 49, 257–271.
Hu, T., Jing, Z., Zhang, Q., Pan, Y., Yuan, M., Li, M., 2025. Shale oil micro–migration characterization: key methods and outlook. Adv. Geo–Energy Res. 15, 5–12.
Huang, H., Larter, S.R., Love, G.D., 2003. Analysis of wax hydrocarbons in petroleum source rocks from the Damintun depression, eastern China, using high temperature gas chromatography. Org. Geochem. 34, 1673–1687.
Huang, H., Zhang, H., Ma, Z., Yang, X., Ma, Y., Zheng, L., 2025. Evolution of pore structure in the Upper Cretaceous Second White Speckled Shale during thermal maturation: insights from artificial and naturally matured samples. Int. J. Coal Geol. 302, 104728.
Jarvie, D.M., 2012. Shale Resource Systems for Oil and Gas: Part 2 – shale–oil Resource Systems, 97. AAPG Memoir, pp. 89–119.
Ji, W., Hao, F., Gong, F., Zhang, J., Bai, Y., Liang, C., Tian, J., 2024. Petroleum migration and accumulation in a shale oil system of the Upper Cretaceous Qingshankou Formation in the Songliao Basin, northeastern China. AAPG Bull. 108, 1611–1648.
Jiang, Z., Li, T., Gong, H., Jiang, T., Chang, J., Ning, C., Su, S., Chen, W., 2020. Characteristics of low–mature shale reservoirs in Zhanhua sag and their influence on the mobility of shale oil. Acta Pet. Sinica 41, 1587–1600 (In Chinese with English abstract).
Jin, Z., Zhu, R., Shen, Y., 2021. Several issues worthy of attention in current lacustrine shale oil exploration and development. Pet. Explor. Develop. 48, 1471–1484.
Johnson, R.C., Birdwell, J.E., Mercier, T.J., Brownfield, M.E., 2016. Geology of Tight Oil and Potential Tight Oil Reservoirs in the Lower Part of the Green River Formation, Uinta, Piceance, and Greater Green River Basins, Utah, Colorado, and Wyoming (No. 2016-5008). US Geological Survey.
Kalani, M., Jahren, J., Mondol, N.H., Faleide, J.I., 2015. Petrophysical implications of source rock microfracturing. Int. J. Coal Geol. 143, 43–67.
Katz, B.J., Lin, F., 2021. Consideration of the limitations of thermal maturity with respect to vitrinite reflectance, Tmax, and other proxies. AAPG Bull. 105, 695–720.
Krooss, B.M., Brothers, L., Engel, M.H., 1991. Geochromatography in Petroleum Migration: a Review, 59. Geological Society, London, Special Publications, pp. 149–163.
Lafargue, E., Marquis, F., Pillot, D., 1998. Rock–Eval 6 applications in hydrocarbon exploration, production, and soil contamination studies. Rev. Inst. Fr. Petrol 53, 421–437.
Leythaeuser, D., Mackenzie, A., Schaefer, R.G., Bjorøy, M., 1984. A novel approach for recognition and quantification of hydrocarbon migration effects in shale–sandstone sequences. AAPG Bull. 68, 196–219.
Li, H., Liu, B., Liu, X., Meng, L., Cheng, L., Wang, H., 2019a. Mineralogy and inorganic geochemistry of the Es4 shales of the Damintun Sag, northeast of the Bohai Bay Basin: implication for depositional environment. Mar. Petrol. Geol. 110, 886–900.
Li, X., Liu, X., Li, J., Tian, Z., 2019b. Comprehensive evaluation and exploration practice of Sha 4 lacustrine shale oil in Damintun sag, Liaohe depression. China Pet. Explor 24, 636–648 (In Chinese with English abstract).
Li, Z., Sun, Z., Li, M., Cao, T., Qian, M., Ma, X., Liu, P., Bao, Y., Jiang, Q., Tao, G., Zhang, J., Rui, X., 2021. Maturity limit of sweet spot area for continental matrix type shale oil: a case study of lower Es 3 and upper Es 4 sub–members in Dongying Sag, Bohai Bay Basin. Pet. Geol. Experi. 43, 767–775 (In Chinese with English abstract).
Li, J., Wang, M., Jiang, C., Lu, S., Li, Z., 2022. Sorption model of lacustrine shale oil: insights from the contribution of organic matter and clay minerals. Energy 260, 125011.
Liu, H., Bao, Y., Zhang, S., Li, Z., Li, J., Wang, X., Wu, L., Wang, Y., Wang, W., Zhu, R., Zhang, S., Wang, X., 2023. Structural characteristics of continental carbonate–rich shale and shale oil movability: a case study of the Paleogene Shahejie Formation shale in Jiyang Depression, Bohai Bay Basin, China. Pet. Explor. Develop. 50, 1320–1332.
Ma, Y., Cai, X., Zhao, P., Hu, Z., Liu, H., Gao, B., Wang, W., Li, Z., Zhang, Z., 2022. Geological characteristics and exploration practices of continental shale oil in China. Acta Geol. Sin. 96, 155–171 (In Chinese with English abstract).
Ma, Y., Yang, C., Li, D., Zhao, H., Pan, Z., Zhou, Y., Zhong, N., 2025. Genetic relationship between shell fossils and shale oil: a case study of Jurassic shale reservoir in the northeast Sichuan Basin. China Geol 8, 360–372.
Malozyomov, B.V., Martyushev, N.V., Kukartsev, V.V., Tynchenko, V.S., Bukhtoyarov, V. V., Wu, X., Tyncheko, Y.A., Kukartsev, V.A., 2023. Overview of methods for enhanced oil recovery from conventional and unconventional reservoirs. Energies 16, 4907.
Mastalerz, M., Schimmelmann, A., Drobniak, A., Chen, Y., 2013. Porosity of Devonian and Mississippian New Albany Shale across a maturation gradient: insights from organic petrology, gas adsorption, and mercury intrusion. AAPG Bull. 97, 1621–1643.
Nalley, S., LaRose, A., 2021. Annual Energy Outlook 2021. US Energy Information Administration.
Nurbekova, R., Smirnova, N., Goncharev, I., Sachsenhofer, R.F., Hazlett, R., Smirnov, G., Yensepbayev, T., Mametov, S., Fustic, M., 2023. High-quality source rocks in an underexplored basin: the upper Carboniferous–Permian succession in the Zaysan Basin (Kazakhstan). Int. J. Coal Geol. 272, 104254.
Peters, K.E., 1986. Guidelines for evaluating petroleum source rock using programmed pyrolysis. AAPG Bull. 70, 318–329.
Raji, M., Gröcke, D.R., Greenwell, H.C., Gluyas, J.G., Cornford, C., 2015. The effect of interbedding on shale reservoir properties. Mar. Petrol. Geol. 67, 154–169.
Salygin, V., Guliev, I., Chernysheva, N., Sokolova, E., Toropova, N., Egorova, L., 2019. Global shale revolution: successes, challenges, and prospects. Sustainability 11, 1627.
Teixeira, M.G., Donzé, F., Renard, F., Panahi, H., Papachristos, E., Scholtès, L., 2017. Microfracturing during primary migration in shales. Tectonophysics 694, 268–279.
Van de Wetering, N., Sanei, H., Mayer, B., 2016. Organic matter characterization in mixed hydrocarbon producing areas within the Duvernay Formation, Western Canada Sedimentary Basin, Alberta. Int. J. Coal Geol. 156, 1–11.
Wang, X., Zhang, G., Tang, W., Wang, D., Wang, K., Liu, J., Du, D., 2022. A review of commercial development of continental shale oil in China. Energy Geosci 3, 282–289.
Wang, W., Wang, X., Li, Z., Wang, Y., Feng, L., Li, P., 2024. Pore and fracture characteristics of low–maturity continental shale and its significance for shale oil occurrence: a case study of Shahejie Formation in Qingnan Sag, Jiyang Depression. Geol. Sci. Technol. Bull. 43, 94–107 (In Chinese with English abstract).

Yang, Y., Zheng, X., Xiao, Y., Lei, Z., Xing, H., Xiong, T., Liu, M., Liu, S., Hou, M., Zhang, Y., 2023. Progress in exploration and development of high–mature shale oil of PetroChina. China Pet. Explor 28, 23–33 (In Chinese with English abstract).
Yang, Y., Zhang, S., Lü, Q., Du Yushan, L.W., Cheng, Z., Lü, J., Liu, Z., 2024. Stereoscopic development techniques for shale oil with low–medium maturity in continental faulted basins in eastern China: a case study of the Paleogene Shahejie Formation in Jiyang Depression. Acta Pet. Sin. 45, 672–682 (In Chinese with English abstract).
Yuan, Y., Rezaee, R., Al–Khdheeawi, E.A., Hu, S.Y., Verrall, M., Zou, J., Liu, K., 2019. Impact of composition on pore structure properties in shale: implications for micro–/mesopore volume and surface area prediction. Energy Fuels 33, 9619–9628.
Zhang, H., Huang, H., Li, Z., Liu, M., 2019. Oil physical status in lacustrine shale reservoirs–A case study on Eocene Shahejie Formation shales, Dongying Depression, East China. Fuel 257, 116027.
Zhang, H., Huang, H., Yin, M., 2022. Investigation on oil physical states of hybrid shale oil System: a case Study on Cretaceous second white speckled shale Formation from highwood River outcrop, Southern Alberta. Minerals 12, 802.
Zhao, W., Hu, S., Hou, L., Yang, T., Li, X., Guo, B., Yang, Z., 2020. Types and resource potential of continental shale oil in China and its boundary with tight oil. Pet. Explor. Development 47, 1–11.
Zou, C., Pan, S., Horsfield, B., Yang, Z., Hao, S., Liu, E., Zhang, L., 2019. Oil retention and intrasource migration in the organic–rich lacustrine Chang 7 shale of the Upper Triassic Yanchang Formation, Ordos Basin, central China. AAPG Bull. 103, 2627–2663.